Theoretical and Experimental Study of Pressure Hysteresis in the Palladium Hydride Phase Transformation

Thesis by

Aadith Moorthy

In Partial Fulfillment of the Requirements for

the degree of

Bachelor of Science

CALIFORNIA INSTITUTE OF TECHNOLOGY

Pasadena, California

2018

Acknowledgements

Several individuals have helped me to compose this senior thesis and carry out its research. My advisor, Prof. Brent Fultz, has probably played the largest role. I have been a member of the Fultz group since late 2015, and since then he has always given me the best advice, on research and in general. For this project, he has offered guidance throughout the process, from advice on the initial experimental approaches and scientific literature to read, to even proofreading this entire thesis over a single weekend. Without his support and encouragement, this work would have not been possible. Next, Nick Weadock, a graduate student in the Fultz group, has also played a large role. It was with his help that much of the physical components of the in-situ x-ray diffraction setup could be assembled. In addition, he has been an expert in aligning the x-ray beam, a crucial but tedious step to ensure that the acquired diffraction patterns are correct. I also appreciate the countless fruitful discussions I have had with him on metal hydride hysteresis theory. I thank the past and present members of the Fultz group for their general advice and support. Finally, I thank my parents for their constant support throughout the research process.

Abstract

A unique phenomenon occurring with metal hydride systems that presents a loss in hydrogen storage efficiency and has received little scientific attention is the hysteresis behavior observed during H_2 absorption and desorption. As an ambient H_2 pressure is introduced into a metal hydride, the material undergoes a phase transformation from a hydrogen-poor phase to a hydrogen-rich phase during absorption and the reverse during desorption. However, the phase transformation is hysteretic as it occurs at a much higher H_2 pressure for absorption than for desorption.

In this work, the thermodynamics of the metal hydride phase transformation with hydrogen uptake are experimentally studied using the palladium-hydride system with in-situ x-ray diffraction. The in-situ x-ray diffraction has enabled the study of the thermodynamic evolution of the microstructure of the palladium through lattice parameters, phase fractions, strain analyses and other information. The diffraction data has then been compared to the predictions from existing theories on hysteresis in metal hydrides, such as the Schwarz-Khachaturyan and Flanagan-Clewley theories. Finally, these theories are extended and combined to form a new general theory of metal hydride phase transformation thermodynamics that incorporates new attributes of importance for practical metal hydride systems, such as phase interface coherency and changes in dislocation formation energies due to work hardening. This new theory is very effective in explaining the prominent trends in the experimental data and provides a highly general approach for the analysis of phase transformations from hydriding in real metals.

Table of Contents

List of Illustrations

Illustration **Page**

Nomenclature

Metal Hydride. Any material that consists of a metallic element, or a compound of metallic elements, and hydrogen

Pressure Hysteresis. The observed difference in hydrogen absorption and desorption pressures observed for certain metal hydrides

Gibbs Free Energy. A thermodynamic variable that is related to a system's energy

Pd. The abbreviation for palladium, an element

PdH. The abbreviation for the material palladium hydride

Phase. A region of a material that has the same material properties

α phase. The hydrogen-poor phase of PdH

β phase. The hydrogen-rich phase of PdH

Chemical Potential. The rate of change of the Gibbs free energy with respect to the number of units in a system

X-ray Diffraction. An experimental method to determine atomic structure of materials with x-rays

Interface. The region where two different materials or two phases of a material are in contact

Interstitial atom. An atom that occupies vacant spaces found in a lattice of other atoms

Lattice Defect. A deviation in a crystal lattice from its periodic nature

Dislocation. A one-dimensional lattice defect which can often be thought of as a plane of atoms that abruptly terminates in a lattice

Lattice Parameter. A length of the unit cell of a crystal lattice, and related to the spacing of atoms

Phase Fraction. The fraction of a given phase present in a material

Strain. A measurement of deformation of a material

Microstrain. The strain multiplied by 10^6

Gradient Boosted Decision Tree. A machine learning model that learns a series of if-then-else statements sequentially from the data

Chapter I

Introduction to Metal Hydrides and Hysteresis

Hydrogen storage is one of the major challenges for the widespread adoption of H_2 as a fuel for vehicular applications. One of the safest and most volume-efficient ways to store H_2 is through metal hydrides [1]. Metals are relatively dense compared to other classes of materials, so their hydrides naturally have very high volumetric energy densities, compared to other hydrogen storage methods. The hydrogen is not present in diatomic form, but rather dissociated into atoms in metal hydride, making them safer than compressed gas storage. Some, metal hydrides absorb and release hydrogen near room temperature, giving them an important advantage for practical application over low-temperature adsorbents materials and cryogenic storage. Finally, it is relatively easy to tune metal alloys by varying their compositions to achieve materials that exhibit a variety of hydrogen uptake characteristics at different temperatures and pressures [2]. All these factors show that metal hydrides are one of the most promising systems for hydrogen storage.

1.1 Properties of Metal Hydrides

A metal hydride can refer to any material that consists of a metallic element, or a compound of metallic elements, and hydrogen. The overall material may be either ionic or a solid solution. For ionic hydrides, the hydrogen atoms are ionically bonded to the metal atoms, resulting in a different chemical structure than for a hydrogen-free material. On the other hand, in the solid solution, the metal may be considered a solvent, and the hydrogen atoms, which will invariably fill interstitial sites, the solute [3]. A metal hydride absorbs hydrogen as the pressure is increased, because the increasing chemical potential of hydrogen gas makes it more favorable for hydrogen to exist in interstitial sites or bonded to the metal. Similarly, desorption occurs as the pressure is decreased. Under some conditions, metal hydrides may undergo a phase transformation during absorption from a hydrogen-poor "α phase" to a hydrogen-rich "β phase", and likewise during

desorption [4]. The β phase typically has a larger lattice parameter than the α phase to accommodate its larger hydrogen concentration. The phase transformation thus allows the metal hydride to absorb more hydrogen. However, due to the two-phase region, the Gibbs free energy is a binodal curve in this regime, and as the temperature is increased, the difference in concentration between the two phases shrinks until a critical temperature is reached where the phase transformation disappears [5]. In addition, certain alloys, like $LaNi_5$, exhibit two-phase behavior near room temperature conditions, but completely lose the phase transition when doped with other materials, such as Cu or Sn, which significantly lower the critical temperature [6].

1.2 Pressure Hysteresis

If typical first-order thermodynamic phase transformation theory were applied to the metal hydride two-phase regime, then the absorption phase transformation would occur at the pressure where the chemical potential of the hydrogen in the α phase equals that of the β phase at a microscopic level. The chemical potentials of each phase would be unaffected by the phase transformation itself, so desorption would also be predicted to occur at the same exact pressure as absorption. However, in reality, as seen in a typical pressure-concentration isotherm for a two-phase metal hydride (Fig 1.1), the absorption occurs at a higher pressure compared to the desorption [5]. Hence, metal hydrides exhibit a pressure hysteresis during hydrogen absorption and desorption. For a typical metal hydride-based hydrogen storage system, this implies that a higher H_2 pressure needs to be used during fueling than the effective pressure that will form while the hydrogen is being released during vehicular operation. This is a thermodynamic loss in efficiency: a fuel cell that uses the hydrogen stored in a metal hydride would work more efficiently at higher hydrogen pressures [7]. This is also a behavior of metal hydrides that has not been explored significantly in a theoretical manner to develop better metal hydrides, and remains a scientific challenge for understanding metal hydride systems [8]. This study attempts to build and extend existing theoretical frameworks for the thermodynamics of metal hydrides to provide a better description for hysteresis, using extensive empirical measurements.

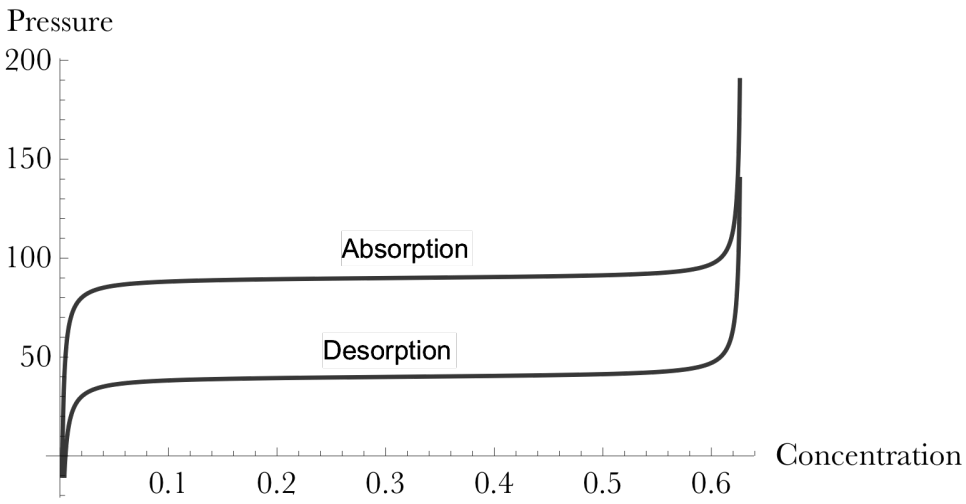

Fig 1.1. Typical metal hydride pressure-concentration isotherm when two phases are present. For low concentrations, below 0.01 in this case, only α phase is present, whereas for high concentrations, above 0.61 in this case, only β phase is present, and both phases coexist in a "two-phase region" for the intermediate regime. The pressure and concentration axes are in arbitrary units to illustrate the general form of these isotherms.

1.3 Evolution of Explanations for Pressure Hysteresis

Hysteresis in metal hydrides has been a topic of scientific interest since the 1930s [9, 10]. Despite this long history, the cause of the hysteresis has remained a debated subject over the course of the last 80 years [8]. The first known explanation for the hysteresis was very qualitative and focused on how the metal hydride system has an additional degree of freedom other than the usual temperature, pressure and hydrogen concentration: mechanical strain in the lattice [9]. The phase with a higher concentration of hydrogen has much more mechanical strain, leading to the difference in absorption and desorption plateau pressures. In particular, it was proposed that the Gibbs phase rule be modified to accommodate this extra inherent degree of freedom. Although not quantitative, this explanation is related to the current Schwarz-Khachaturyan theory of hysteresis, as shall be seen below.

Later it was even proposed that the hysteresis occurs because the chemical potentials of both phases of the metal hydride are not truly equal at the plateau, because of the poor kinetics of metal atoms [10]. This explanation is probably unlikely due to the lack of any measurable change to the hysteresis gap during metal hydride cycling even after long equilibration times of 100+ hours.

Since as early as the 1960s, several people in the field have ascribed the hysteresis to the occurrence of plastic deformation in the forming phase during the absorption phase transformation [10-13]. The general argument is that the energy associated with the creation of dislocations due to plastic deformation must be overcome to initiate the phase transformation, resulting in an elevated pressure for the absorption plateau. Over two decades, this explanation was incrementally improved, until Flanagan and Clewley formalized it into a quantitative theory of hysteresis in 1982 [14]. The Flanagan-Clewley theory is presented in more detail and extended in Ch 3.

There have also been efforts to understand the coherency strains that occur due to the misfit of the crystal lattice. This misfit occurs from the interstitial hydrogen atoms and this explanation is similar to the aforementioned efforts in the 1930s. These strain-based approaches were formalized in 1995 by Schwarz and Khachaturyan to produce a theory of hysteresis that is wholly dependent on the strains produced by misfitting hydrogen interstitials for phases that have coherent interfaces [15, 16]. The Schwarz-Khachaturyan theory is presented in more detail and extended in Ch 2.

The Schwarz-Khachaturyan theory and the Flanagan-Clewley theory are the two predominant theories of hysteresis today, and it remains a matter of scientific research to determine which theory provides a better description of experimental measurements of hysteresis in real metal hydride systems [8].

In the past decade, work on understanding metal hydride systems has significantly shifted to analyses of the hydrogen uptake properties of nanoparticles [17-19]. For nanoparticles, the plastic deformation is assumed to be minimal, so the main consideration is the strain energy due to the misfitting solute atoms – the hydrogen interstitials. However, the behavior of nanoparticles upon hydrogen uptake is completely different from the bulk material behavior and does not provide a useful connection to

study the causes of hysteresis in bulk systems. In particular, at the nanoparticle level, the phase transformation itself seems to collapse into a gradual increase in hydrogen concentration for a single phase, as opposed to an equilibrium between two phases that have somewhat constant concentrations [17]. A "hysteresis gap" still exists between absorption and desorption for the nanoparticles, but cannot be understood in the same way as for a bulk material: the gap between two phase transformations. Yet, nanoparticles may provide insight on how the Schwarz-Khachaturyan or Flanagan-Clewley theories may be altered by changes in particle size to the extreme scale of nanoparticles.

1.4 Thesis Outline and Background

The focus of this study is to understand the origins of hysteresis by comparing experimental results to the existing theories, and then extending these theories to provide a new general theory of hysteresis to accurately describe all the behaviors related to the hysteresis of metal hydrides.

The palladium hydride (PdH) system is chosen for experimental evaluation, because there are several experimental benefits to using palladium (Pd). Pd has a Face-Centered Cubic (FCC) lattice structure, in both its α and β phase [20]. The phases thus have high symmetry lattice structures and also approximately follow Vegard's law – these are the key assumptions of the Schwarz-Khachaturyan model. Additionally, Pd is very effective at storing hydrogen – it can store nearly 900 times its own volume in H_2 at room temperature [21]. Pd also has absorption and desorption plateaus that occur at pressures that are easily measurable in a typical pressure chamber. For example, at 60°C, the absorption plateau is around 90 torr and the desorption plateau is around 40 torr [18]. 60°C is well below the critical temperature mentioned earlier, beyond which no phase transformation occurs [20]. Finally, the kinetics of hydrogen absorption and desorption in palladium are fast, and reversible, enabling the study of thermodynamics in the system. This is particularly true because palladium is an effective catalyst for hydrogen dissociation from diatomic gas to single interstitial atoms, which is often the rate-limiting step for hydrogen uptake in several metal hydride systems [22].

Despite being called "palladium hydride", the PdH system does not have ionic bonding and is instead best described as a solid solution, where the Pd lattice is the solvent and the interstitial hydrogen atoms are the solute [20]. The hydrogen atoms occupy the octahedral interstitial sites [23]. In the α phase, the fraction of interstitial sites occupied by hydrogen atoms is about 0.04 at 60°C, whereas it is close to 0.55 at 60°C in the β phases [18]. To accommodate this increase in hydrogen concentration, the α phase lattice parameter is 3.89 Å but that of the β phase is 4.04 Å, a volume expansion of approximately 12% [20].

In this study, in-situ x-ray diffraction has been chosen as the primary method of characterization. Hydrogen gas is allowed to equilibrate with the metal hydride, and diffraction profiles are acquired to analyze the evolving microstructure of the material with hydrogen uptake. X-ray diffraction is particularly powerful because it allows determinations of lattice parameters, phase fractions, internal strains and other microstructural properties that can reveal how metal hydrides are altered by the presence of hydrogen interstitials at various concentrations. In-situ x-ray diffraction has been successfully used to study metal hydrides, and even the specific PdH system, to uncover properties of the phase transformation [6, 24]. Hence, in this study, the derived datasets from in-situ x-ray diffraction are directly connected to the predictions of the existing theories of hysteresis, for their experimental verification and extension. The experimental setup and data analysis methods are described in more detail in Ch 4, 5 and 6.

1.5 Chapter References

1. Rusman, N. & Dahari, M. A review on the current progress of metal hydrides material for solid-state hydrogen storage applications. *International Journal of Hydrogen Energy* 41, 12108-12126 (2016).
2. Lototskyy, M. et al. The use of metal hydrides in fuel cell applications. *Progress in Natural Science: Materials International* 27, 3-20 (2017).
3. Libowitz, G. The nature and properties of transition metal hydrides. *Journal of Nuclear Materials* 2, 1-22 (1960).
4. Wipf, H. et al. *Hydrogen in Metals III*. 279-340 (Springer Berlin, 2014).
5. Huang, W. et al. Experimental observation of hysteresis in a coherent metal-hydride phase transition. *Journal of Physics: Condensed Matter* 29, 495701 (2017).

6. Notten, P., Daams, J. & Einerhand, R. On the nature of the electrochemical cycling stability of non-stoichiometric LaNi5-based hydride-forming compounds Part II. In situ x-ray diffractometry. *Journal of Alloys and Compounds* 210, 233-241 (1994).
7. Bove, R. *Modeling solid oxide fuel cells*. 13-50 (Springer, 2014).
8. Puls, M. Theories of Coherent Phase Equilibrium. *The Effect of Hydrogen and Hydrides on the Integrity of Zirconium Alloy Components* 207-242 (2012). doi:10.1007/978-1-4471-4195-2_7
9. Ubbelohde, A. Some Properties of the Metallic State. I. Metallic Hydrogen and Its Alloys. *Proceedings of the Royal Society A: Mathematical, Physical and Engineering Sciences*159, 295-306 (1937).
10. Scholtus, N. & Hall, W. Hysteresis in the Palladium—Hydrogen System. *The Journal of Chemical Physics* 39, 868-870 (1963).
11. Andresen, A. & Maeland, A. *Hydrides for energy storage*. 395-396 (Pergamon Press, 1978).
12. Paton, N., Hickman, B. & Leslie, D. Behavior of hydrogen in α-phase Ti-Al alloys. *Metallurgical Transactions* 2, 2791-2796 (1971).
13. Gahr, S. & Birnbaum, H. Hydrogen embrittlement of niobium—III. High temperature behavior. *Acta Metallurgica* 26, 1781-1788 (1978).
14. Flanagan, T. & Clewley, J. Hysteresis in metal hydrides. *Journal of the Less Common Metals.* 83, 127-141 (1982).
15. Schwarz, R. & Khachaturyan, A. Thermodynamics of Open Two-Phase Systems with Coherent Interfaces. *Physical Review Letters* 74, 2523-2526 (1995).
16. Schwarz, R. & Khachaturyan, A. Thermodynamics of open two-phase systems with coherent interfaces: Application to metal–hydrogen systems. *Acta Materialia* 54, 313-323 (2006).
17. Griessen, R., Strohfeldt, N. & Giessen, H. Thermodynamics of the hybrid interaction of hydrogen with palladium nanoparticles. *Nature Materials* 15, 311-317 (2015).
18. Syrenova, S. et al. Hydride formation thermodynamics and hysteresis in individual Pd nanocrystals with different size and shape. *Nature Materials* 14, 1236-1244 (2015).
19. Wadell, C. et al. Thermodynamics of hydride formation and decomposition in supported sub-10nm Pd nanoparticles of different sizes. *Chemical Physics Letters* 603, 75-81 (2014).
20. Conway, B. & Jerkiewicz, G. *Proceedings of the Symposium on Electrochemistry and Materials Science of Cathodic Hydrogen Absorption and Adsorption*. 17-26 (Electrochemical Society, 1995).
21. Chen, Z. et al. Applications of silicon nanowires functionalized with palladium nanoparticles in hydrogen sensors. *Nanotechnology* 18, 345502 (2007).
22. Adams, B. & Chen, A. The role of palladium in a hydrogen economy. *Materials Today* 14, 282-289 (2011).
23. Akiba, H. et al. Nanometer-Size Effect on Hydrogen Sites in Palladium Lattice. *Journal of the American Chemical Society* 138, 10238-10243 (2016).
24. Kawasaki, A. et al. Change in the crystalline structure during the phase transition of the palladium–hydrogen system. *Phys. Chem. Chem. Phys.* 17, 24783-24790 (2015).

Chapter II

Schwarz-Khachaturyan Theory of Hysteresis in Metal Hydride Systems

The Schwarz-Khachaturyan Theory explains the origins of hysteresis in metal hydride systems with coherent phase transformations. It utilizes the inherent strain energy associated with the insertion of hydrogen atoms into interstitial sites in the metal lattice [1-3].

2.1 Nature of Interfaces

An interface between two phases is said to be coherent when they are able to match their lattices perfectly at the interface. This enables the overall lattice to be effectively continuous over the entire interface. On the other hand, two phases may be incoherent at the interface if the lattice is completely discontinuous at the interface. It is typically observed that phase transformations are coherent when the lattice parameter change between the two phases is within 1% [4]. For scenarios where the lattice parameter change is greater than 25%, the interface is considered to be incoherent. In the intermediate region, the interface is called 'semi-coherent'. As mentioned before, the Schwarz-Khachaturyan Theory, as originally presented, is strictly a derivation for phase transformations that occur with coherent interfaces.

2.2 Eshelby Theory

The strain energy accompanied by the insertion of 'misfitting' atoms into interstitial sites was derived by J. D. Eshelby in 1956, as part of a continuum theory of lattice defects [5]. The stresses experienced by interstitial atoms are understood using a sphere-in-hole model. The 'misfitting' atom is larger in volume outside of the lattice than the total volume of the vacant interstitial site, resulting in the Eshelby strain. When the atom is inserted into the site, the resulting volume of the filled site is an intermediate value between that of the atom outside of the lattice and that of the vacant interstitial site. Let

the volume change experienced by the interstitial atom, compared to its volume outside of the lattice be ΔV_a, and that of the filled interstitial site compared to the vacant site be ΔV_s. Then, we can use the general form of the energy due to a strain in a material to represent the elastic energy of the interstitial atom and site respectively, relative to the pristine, inclusion-free material.

$$E_s = \frac{1}{2} V_s Y \epsilon_s^2 = \frac{1}{2} V_s \mathrm{Y} \left(\frac{\Delta V_s}{V_s}\right)^2 = \frac{\mathrm{Y} \Delta V_s^2}{2\, V_s} \tag{2.1}$$

$$E_a = \frac{1}{2} V_a Y \epsilon_a^2 = \frac{1}{2} V_a \mathrm{Y} \left(\frac{\Delta V_a}{V_a}\right)^2 = \frac{\mathrm{Y} \Delta V_a^2}{2\, V_a} \tag{2.2}$$

where Y is the Young's Modulus.

In the case of metal hydride systems, it is the hydrogen atoms that are at interstitial sites and are considered to be the 'misfitting' atoms. For example, hydrogen atoms themselves have a volume of $0.62 Å^3$, leading to a strong misfitting strain in the PdH system as there is a final volume of just $0.27 Å^3$ for the filled interstitial site [6]. Schwarz and Khachaturyan use this strain to derive a hysteretic gap in the phase transformation [1].

Considering the total strain energies throughout the lattice in this manner outlined above, Eshelby derives a simplified expression for the elastic energy arising from misfitting interstitial atoms:

$$E_{el} = 2N v_0 G_s \frac{1+\sigma}{1-\sigma} \varepsilon_0^2 \bar{c}(1-\bar{c}) \tag{2.3}$$

where v_0 is the volume occupied by the atom in the interstitial site, G_s is the shear modulus, σ the Poisson ratio, N the number of interstitial sites, $\bar{c}$ the fraction of total interstitial sites that are filled and ε_0, a term that linearly relates solid solution composition to lattice parameter, as given by Vegard's law. In the case of an interstitial solution, as in metal hydrides, Vegard's law simplifies to:

$$a = (1 + \varepsilon_0 \bar{c}) a^0 \tag{2.4}$$

where a is the predicted lattice parameter for a crystal with interstitials, given a lattice parameter of a^0 for a pristine lattice free of interstitials. Vegard's law is not a completely general model of the variation of lattice parameter with hydrogen concentration in metal

hydrides. However, it is a powerful simplifying assumption in the thermodynamic calculations that ensue. It also turns out to often be correct or at least very close to correct within measurable accuracy for several systems, including PdH, as shall be examined in Ch 7. The multiplicative factor $2v_0\varepsilon_0^2 G_s \frac{1+\sigma}{1-\sigma}$ primarily consists of material properties, and is abbreviated as A in the subsequent discussion for brevity:

$$E_{el} = NA\bar{c}(1-\bar{c}) \tag{2.5}$$

$$e_{el} = A\bar{c}(1-\bar{c}) \tag{2.6}$$

2.3 Strain Energy Components for two-phase metal hydride systems

Assuming the veracity of Vegard's law, the lattice parameters in the α and β phases during the 2-phase region of a phase transformation are:

$$a_\alpha = (1+\varepsilon_0 c_\alpha)a_\alpha^0 \tag{2.7}$$

$$a_\beta = \left(1+\varepsilon_0 c_\beta\right)a_\beta^0 \tag{2.8}$$

where c_α is the fraction of total interstitial sites that are filled in the α phase, c_β that for the β phase, a_α^0 the lattice parameter of the α phase at $c_\alpha = 0$ and a_β^0 similarly for the β phase.

The fractional change in lattice parameter from α to β phase can then be quantified, with the assumption that their difference is small:

$$\varepsilon = \frac{a_\beta - a_\alpha}{a_\alpha} \approx \frac{a_\alpha^0\,\varepsilon_0\left(c_\beta - c_\alpha\right)}{(1+\varepsilon_0 c_\alpha)a_\alpha^0} \approx \varepsilon_0\left(c_\beta - c_\alpha\right) \tag{2.9}$$

This quantity is important while considering the strain energy caused by the constraining of one phase by another phase. For example, during absorption in metal hydrides, the β phase is the forming phase, and is elastically constrained by the α phase. This behavior results in a strain energy, as observed by Schwarz and Khachaturyan, of:

$$e_{\frac{\alpha}{\beta}} = 2Nv_0 G_s \frac{1+\sigma}{1-\sigma}\varepsilon^2\omega(1-\omega) \tag{2.10}$$

where ω is the extent of the transformation or equivalently the β phase fraction. Specifically, ω may be expressed in terms of concentration by the lever rule as:

$$\omega = \frac{\bar{c} - c_\alpha}{c_\beta - c_\alpha} \tag{2.11}$$

Using the constant A and the previously derived relation for ε, we may re-express $e_{\alpha/\beta}$:

$$e_{\frac{\alpha}{\beta}} = A\left(c_\beta - c_\alpha\right)^2 \omega(1-\omega) \tag{2.12}$$

In addition to this strain, the α and β phases have their own misfitting particle strains in the same form as that of Eshelby's original formulation. This gives a total strain energy of:

$$\begin{aligned} e_{tot} &= e_\alpha + e_\beta + e_{\frac{\alpha}{\beta}} \\ &= Ac_\alpha(1-c_\alpha)\omega + Ac_\beta\left(1-c_\beta\right)(1-\omega) + A\left(c_\beta - c_\alpha\right)^2 \omega(1-\omega) \end{aligned} \tag{2.13}$$

Upon simplifying using the previously noted expression for ω, an interesting result arises:

$$e_{tot} = A\bar{c}(1-\bar{c}) \tag{2.14}$$

This expression is identical to the naïve application of Eshelby's strain energy result to the entire interstitial solution system, only taking into account the total fraction of interstitial sites that are occupied and some general material properties. Most notably, the expression is completely independent of the phase fractions of either phase. This result is formalized in the Bitter-Crum theorem, which states that if two phases have similar elastic properties and have coherent interfaces, the total elastic energy is independent of the shape or distribution of the phases [3]. In the case of metal hydrides, the differential distribution of the interstitial hydrogen atoms in the α and β phases does not affect the total elastic energy, which only depends on their concentration.

2.4 Thermodynamics of the Metal Hydride System

With the results of the previous sections, it is now possible to write thermodynamic expressions to describe the metal hydride system. First, consider the total Gibbs free energy when a metal hydride is purely in the α phase:

$$g_\alpha(c) = g_{chem,\alpha}(c) + e_\alpha = g_{chem,\alpha}(c) + Ac(1-c) \tag{2.15}$$

where $g_{chem,\alpha}$ is the chemical contribution to the free energy of the α phase, and e_α is the misfitting interstitial strain contribution. The expression is similar for the β phase:

$$g_\beta(c) = g_{chem,\beta}(c) + e_\beta = g_{chem,\beta}(c) + Ac(1-c) \tag{2.16}$$

where $g_{chem,\beta}$ is now the chemical contribution to the free energy of the β phase, and e_β is the misfitting interstitial strain contribution. In the two-phase region, the total chemical and strain contributions of each phase and the constraining of one phase by another, must be accounted for, so the total Gibbs free energy is:

$$\begin{aligned} g_{2ph}(\bar{c}) &= g_{chem,\alpha}(c_\alpha)(1-\omega) + g_{chem,\beta}(c_\beta)\omega + e_\alpha + e_\beta + e_{\frac{\alpha}{\beta}} \\ &= g_{chem,\alpha}(c_\alpha)(1-\omega) + g_{chem,\beta}(c_\beta)\omega + A\bar{c}(1-\bar{c}) \end{aligned} \tag{2.17}$$

The chemical potential of the α phase throughout the transition is given by:

$$\mu_\alpha(c_\alpha) = \frac{dg_\alpha(c)}{dc_\alpha} = \frac{dg_{chem,\alpha}(c_\alpha)}{dc_\alpha} + A(1-2c_\alpha) \tag{2.18}$$

Similarly, for the β phase:

$$\mu_\beta(c_\beta) = \frac{dg_\beta(c)}{dc_\beta} = \frac{dg_{chem,\beta}(c_\beta)}{dc_\beta} + A(1-2c_\beta) \tag{2.19}$$

Finally, in the two-phase region the chemical potential is:

$$\begin{aligned} \mu_{2ph}(\bar{c}) = \frac{dg_{2ph}(\bar{c})}{d\bar{c}} &= \left(g_{chem,\beta}(c_\beta) - g_{chem,\alpha}(c_\alpha)\right)\frac{d\omega}{dc} + A(1-2\bar{c}) \\ &= \frac{\left(g_{chem,\beta}(c_\beta) - g_{chem,\alpha}(c_\alpha)\right)}{c_\beta - c_\alpha} + A(1-2\bar{c}) \end{aligned} \tag{2.20}$$

Observe that $\frac{\left(g_{chem,\beta}(c_\beta)-g_{chem,\alpha}(c_\alpha)\right)}{c_\beta-c_\alpha}$ and A are constants in the two-phase region equilibrium. Hence the presence of the strain energy predicts a chemical potential of negative slope in the two-phase region. Due to the continuity of the chemical potential over the entire range, the chemical potential at every point in time can be calculated in this manner, and is graphically shown in Fig. 2.1:

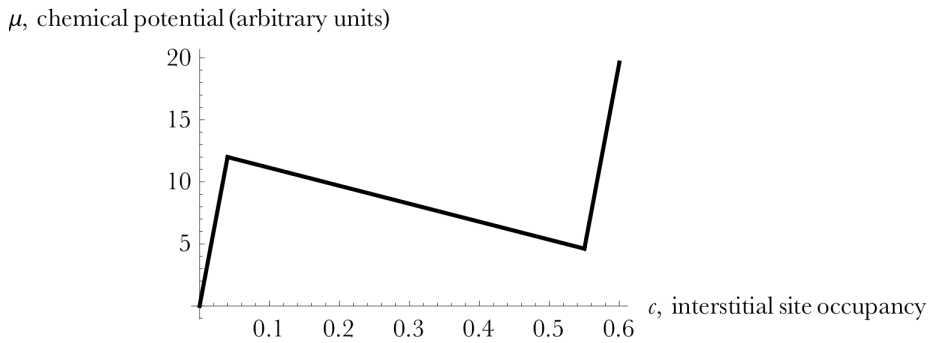

Fig 2.1. Chemical potential of metal hydride system predicted by the Schwarz Khachaturyan theory. The points that are kinks in the graph correspond to the chemical potentials of α and β phases at chemical equilibrium.

2.5 Explanation and Formulation of Pressure Hysteresis

From examining Fig 2.1, the origin and mechanism of the pressure hysteresis is now clear. The pressure of the hydrogen gas is directly related to the chemical potential:

$$\mu_g = \mu_g^0 + \frac{1}{2}kT\ln\left(\frac{p_g}{p_g^0}\right) \tag{2.21}$$

where μ_g^0 and p_g^0 are the chemical potential and pressure at some reference state, p_g the pressure of the gas and μ_g its corresponding chemical potential. Using Fig 2.1 and this relation, the pressure hysteresis can be described. Near vacuum, the metal hydride is composed of purely the α phase. As the pressure of hydrogen gas is increased, the chemical potential of the gas, μ_g, also increases as given above. Let c_α^* and c_β^* be the compositions of the α and β phases at chemical equilibrium. Then, during absorption, only α phase can exist in the regime of $\mu_g < \mu_\alpha(c_\alpha^*)$. However, note that as seen in Fig 2.1, $\mu_\beta(c_\beta^*) < \mu_\alpha(c_\alpha^*)$. The system may be in either phase in the regime $\mu_\beta(c_\beta^*) < \mu_g < \mu_\alpha(c_\alpha^*)$, but since the system is undergoing absorption, no β phase has formed yet. Then, at $\mu_g = \mu_\alpha(c_\alpha^*)$, the chemical potential is now high enough to begin the phase transformation, and α phase starts to become unstable. At equilibrium during a phase transformation, the chemical potentials of each phase must be equal for a given species. Since $\mu_\beta(c_\beta^*) < \mu_\alpha(c_\alpha^*)$, the forming β phase cannot have composition c_β^*. Rather, it will have a higher composition c_β' such that

$$\mu_g = \mu_\beta(c_\beta') = \mu_\alpha(c_\alpha^*) \tag{2.22}$$

satisfying the necessary equilibrium conditions for the chemical potential. In accordance with typical phase transformation theory, as α phase transforms to β phase, the absorption pressure is predicted to be constant. Then, once the transformation is complete, there is purely β phase. Additional increases in pressure result in increases in the number of interstitial hydrogen atoms in the β phase. This same reasoning may be

applied in reverse to develop the desorption transformation's equilibrium condition in the two-phase regime:

$$\mu_g = \mu_\beta\left(c_\beta^*\right) = \mu_\alpha(c'_\alpha) \tag{2.23}$$

where $c'_\alpha < c^*_\alpha$ is the composition of α phase that forms to maintain the chemical potential equilibrium condition.

Now, to quantify the hysteresis gap, consider the difference in the chemical potentials at chemical equilibrium, $\mu_\beta\left(c_\beta^*\right)$ and $\mu_\alpha(c_\alpha^*)$.

$$\mu_\alpha(c_\alpha^*) - \mu_\beta\left(c_\beta^*\right)$$
$$= \frac{dg_{chem,\alpha}(c_\alpha^*)}{dc_\alpha} + A(1-2c_\alpha^*) - \left(\frac{dg_{chem,\beta}\left(c_\beta^*\right)}{dc_\beta} + A\left(1-2c_\beta^*\right)\right) \tag{2.24}$$

From the equilibrium of the chemical contribution to the chemical potential under these conditions, $\frac{dg_{chem,\alpha}(c_\alpha)}{dc_\alpha} = \frac{dg_{chem,\beta}(c_\beta)}{dc_\beta}$. Hence,

$$\mu_\alpha(c_\alpha^*) - \mu_\beta\left(c_\beta^*\right) = 2A\left(c_\beta^* - c_\alpha^*\right) \tag{2.25}$$

Using the relationship of these chemical potentials to gas pressures as mentioned before,

$$\frac{1}{2}kT\ln\left(\frac{p_g^{abs}}{p_g^{des}}\right) = \mu_\alpha(c_\alpha^*) - \mu_\beta\left(c_\beta^*\right) = 2A(c_\beta^* - c_\alpha^*)$$
$$\ln\left(\frac{p_g^{abs}}{p_g^{des}}\right) = \frac{4A\left(c_\beta^* - c_\alpha^*\right)}{kT} = 8v_0G_s\varepsilon_0^2\frac{1+\sigma}{1-\sigma}\frac{\left(c_\beta^* - c_\alpha^*\right)}{kT} \tag{2.26}$$

where p_g^{abs} is the absorption plateau pressure in the two-phase region and p_g^{des} is the desorption plateau pressure.

2.6 Beyond Schwarz-Khachaturyan Theory

Schwarz and Khachaturyan make several simplifying assumptions, and many of them are valid approximations across several practical systems, such as Vegard's law. However, there are a few that are worth reconsidering in more detail for a thorough picture of hysteresis.

Earlier, the constant A was defined:

$$A = 2v_0\varepsilon_0^2G_s\frac{1+\sigma}{1-\sigma} \tag{2.27}$$

It is reasonable to consider that the shear modulus, G_s, and Poisson's ratio, σ, are both material constants and quite similar in both the α and β phases. This is definitely close to correct in Pd where both have an FCC structure with slightly offset lattice parameters, and material constants arise significantly from the properties of the host palladium lattice. However, the same is not necessarily true of v_0, the volume occupied by the hydrogen atom in the interstitial site. This is also pointed out by Eshelby [5]. v_0 is a function of the phase fraction in the two-phase region. In the case of palladium and other materials, this is a significant observable change in volume. For palladium, the α phase lattice parameter is 3.89 Å but that of the β phase is 4.04 Å [7]. This corresponds to a 3.9% lattice parameter increase from α to β phase, and an appreciable volume increase of 12%. This variation only affects the $e_{\alpha/\beta}$ term, which quantifies the elastic constraining of one phase by another. A correct expression for v_0 would have the form:

$$v_0 = v_{0,1}\,(1-\omega) + v_{0,2}\omega \tag{2.28}$$

where $v_{0,1}$ is the volume occupied by the hydrogen atom in the interstitial site of the α phase, and $v_{0,2}$ the corresponding volume for the β phase. This correction to the elastic energy primarily affects the combined chemical potential in the two-phase region. The regime no longer has a linear chemical potential with concentration, but a quadratic one. However, it is verified by taking the first derivative that the chemical potential is still negative sloping. The final effect of this behavior is that the chemical potential drops more rapidly at higher concentrations than at lower ones during the phase transformation. The hysteresis gap would then be slightly larger than predicted with the assumption of a linear chemical potential in the two-phase region.

In several real metal hydride systems, the phase transformation may not be completely coherent. In Pd, as mentioned before, there is a 3.9% lattice parameter increase from α to β phase. As noted at the very beginning of the chapter, this increase falls in the intermediate range, between 1% and 25%, corresponding to semi-coherent transformations. The interface between the two phases is still relatively continuous, but there are some geometrically necessary dislocations formed to facilitate the lattice parameter shift from 3.89 Å to 4.04 Å. For the Schwarz Khachaturyan theory, this

corresponds to a weakening of the $e_{\alpha/\beta}$ term, the energy corresponding to the elastic constraining of one phase by another. For an incoherent interface, this entire term would disappear. Hence, an additional variable, ϕ, is introduced to quantify the nature of the interface. $\phi = 0$ corresponds to an incoherent interface and $\phi = 1$ a perfectly coherent interface. With ϕ, the free energy of the two-phase region is:

$$g_{2ph}(\bar{c}) = g_{chem,\alpha}(c_\alpha)(1-\omega) + g_{chem,\beta}(c_\beta)\omega + e_\alpha + e_\beta + e_{\frac{\alpha}{\beta}}\phi \qquad (2.29)$$

Observe that for an incoherent system, $\phi = 0$ leads to $g_{2ph}(\bar{c}) = g_{chem,\alpha}(c_\alpha)(1-\omega) + g_{chem,\beta}(c_\beta)\omega + e_\alpha + e_\beta$, and the free energy is completely independent of $\bar{c}$ for the two-phase region, leading to no hysteresis.

For $\phi \neq 0$, the chemical potential in the two-phase region has a negative slope whose magnitude is mediated by the ϕ. This effect then tends to reduce the size of the hysteresis gap in real systems. Since ϕ tunes the size of the hysteresis gap from 0 to its maximum possible value, it is a stronger effect that the change in v_0 for most real systems, which tend to have semi-coherent interfaces.

Finally, the Schwarz-Khachaturyan theory assumes a perfect lattice free of defects like lattice site vacancies and dislocations. However, the same 'misfitting particle' strains that are used to explain the hysteresis may also lead to defect formation, leading to a more complicated system. In fact, before Schwarz and Khachaturyan published their theory, the predominant explanation for hysteresis came from the work of Flanagan and Clewley, who exclusively attribute it to dislocations. This is the subject of the next chapter.

2.7 Chapter References

1. Schwarz, R. & Khachaturyan, A. Thermodynamics of Open Two-Phase Systems with Coherent Interfaces. *Physical Review Letters* 74, 2523-2526 (1995).
2. Schwarz, R. & Khachaturyan, A. Thermodynamics of open two-phase systems with coherent interfaces: Application to metal–hydrogen systems. *Acta Materialia* 54, 313-323 (2006).
3. Fultz, B. *Phase transitions in materials*. (Cambridge University Press).
4. Zang, L. *Types of Interfaces: coherent, semi-coherent, and incoherent*. at <http://www.eng.utah.edu/~lzang/images/lecture-21.pdf>

5. Eshelby, J. The Continuum Theory of Lattice Defects. *Solid State Physics* 79-144 (1956). doi:10.1016/s0081-1947(08)60132-0
6. Syrenova, S. et al. Hydride formation thermodynamics and hysteresis in individual Pd nanocrystals with different size and shape. *Nature Materials* 14, 1236-1244 (2015).
7. Conway, B. & Jerkiewicz, G. *Proceedings of the Symposium on Electrochemistry and Materials Science of Cathodic Hydrogen Absorption and Adsorption*. 17-26 (Electrochemical Society, 1995).

Chapter III

Flanagan-Clewley Theory of Hysteresis in Metal Hydride Systems

The Flanagan-Clewley theory explains the origins of hysteresis in metal hydride systems by utilizing the energy required to form dislocations during the phase transformation [1, 2].

The dislocations that may be formed during phase transformations can be of two forms: dislocations formed at interfaces to separate the two phases, and other strain-induced dislocations in the bulk of either phase. The strain-induced bulk dislocations may be formed due to the strains created by inserting hydrogen atoms into interstitial sites. This effect is alluded to in the previous chapter. However, the Flanagan-Clewley theory assumes a relatively strain-free lattice, in opposition to the model of the Schwarz-Khachaturyan theory [1].

3.1 Contribution of Dislocation Formation Energies

According to Flanagan and Clewley, the hysteresis gap opens up due to the energy required to form dislocations during the phase transformation [1]. In particular, dislocations are produced in the forming phase: during absorption, dislocations are produced in the β phase whereas during desorption, they are produced in the α phase.

Using this information, thermodynamic properties for the system may be derived. The formation of dislocations only in the forming phase causes a different Gibbs free energy expression for the absorption two-phase region compared to the desorption two-phase region. Before deriving the Gibbs free energy, consider the total energy of dislocation formation. It is proportional to the extent of reaction, since it is created in the forming phase during the transformation, and has the following form for absorption:

$$e_{disl,abs} = \Delta h_{disl}\, \omega \tag{3.1}$$

where $\omega = \frac{\bar{c}-c_\alpha}{c_\beta-c_\alpha}$ is the phase fraction of the β phase or the extent of the absorption phase transformation and Δh_{disl} is the enthalpy of dislocation production for a unit of the transformation. Flanagan-Clewley theory assumes that Δh_{disl} has no hydrogen concentration dependence for simplicity. Similarly, for desorption, the total energy of dislocation formation is:

$$e_{disl,des} = \Delta h_{disl}\,(1-\omega) \tag{3.2}$$

Here, $1-\omega$ represents the extent of phase transformation, and the phase fraction of α phase.

3.2 Thermodynamics of the Metal Hydride System

Now, Gibbs free energies can be derived. For absorption in the two-phase region:

$$\begin{aligned} g_{2ph,abs} &= g_{chem,\alpha}(c_\alpha)(1-\omega) + g_{chem,\beta}(c_\beta)\omega + e_{disl,abs} \\ &= g_{chem,\alpha}(c_\alpha)(1-\omega) + g_{chem,\beta}(c_\beta)\omega + \Delta h_{disl}\,\omega \end{aligned} \tag{3.3}$$

where $g_{chem,\alpha}$ and $g_{chem,\beta}$ are the chemical contributions to the free energy for the α and β phases. Similarly, for desorption in the two-phase region:

$$\begin{aligned} g_{2ph,des} &= g_{chem,\alpha}(c_\alpha)(1-\omega) + g_{chem,\beta}(c_\beta)\omega + e_{disl,des} \\ &= g_{chem,\alpha}(c_\alpha)(1-\omega) + g_{chem,\beta}(c_\beta)\omega + \Delta h_{disl}\,(1-\omega) \end{aligned} \tag{3.4}$$

The chemical potential is the derivative of the Gibbs free energy with respect to the filled fraction of hydrogen interstitial sites in this system. In the two-phase region, during absorption, the chemical potential is:

$$\begin{aligned} \mu_{2ph,abs}(\bar{c}) &= \frac{dg_{2ph,abs}(\bar{c})}{d\bar{c}} = \left(g_{chem,\beta}(c_\beta) - g_{chem,\alpha}(c_\alpha)\right)\frac{d\omega}{dc} + \Delta h_{disl}\frac{d\omega}{dc} \\ &= \frac{1}{c_\beta - c_\alpha}\left(g_{chem,\beta}(c_\beta) - g_{chem,\alpha}(c_\alpha) + \Delta h_{disl}\right) \end{aligned} \tag{3.5}$$

In the two-phase region, during desorption, the chemical potential is:

$$\begin{aligned} \mu_{2ph,des}(\bar{c}) &= \frac{dg_{2ph,abs}(\bar{c})}{d\bar{c}} = \left(g_{chem,\beta}(c_\beta) - g_{chem,\alpha}(c_\alpha)\right)\frac{d\omega}{dc} - \Delta h_{disl}\frac{d\omega}{dc} \\ &= \frac{1}{c_\beta - c_\alpha}\left(g_{chem,\beta}(c_\beta) - g_{chem,\alpha}(c_\alpha) - \Delta h_{disl}\right) \end{aligned} \tag{3.6}$$

Observe that $\mu_{2ph,abs}(\bar{c})$ and $\mu_{2ph,des}(\bar{c})$ are both constants independent of $\bar{c}$, as expected for a typical phase transformation's equilibrium condition. However, given that $\Delta h_{disl} > 0$, which would be the case in the system initialized by the Flanagan-Clewley theory as free of other internal strains, $\mu_{2ph,abs}(\bar{c}) > \mu_{2ph,des}(\bar{c})$. Hence, absorption is occurring at a different, higher chemical potential than desorption, due to the energy of dislocations. A graph of the variation of chemical potential with hydrogen uptake can now be constructed, and is shown in Fig 3.1.

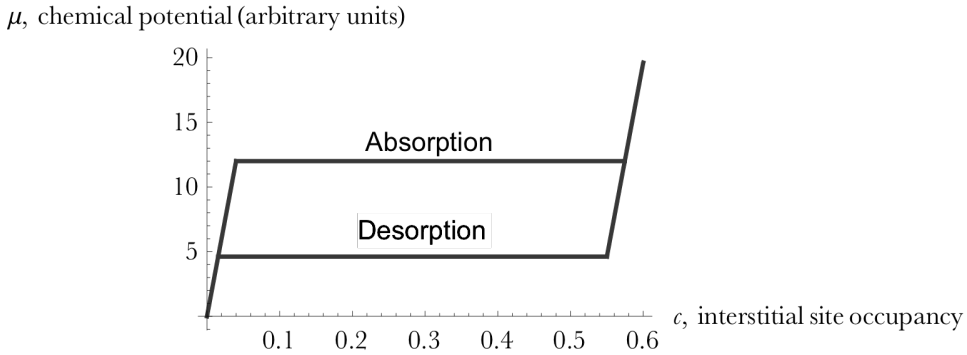

Fig 3.1. Chemical potential of metal hydride system predicted by the Flanagan-Clewley theory. Compare this trend with Fig 2.1 for the Schwarz-Khachaturyan Theory.

3.3 Explanation and Formulation of Pressure Hysteresis

Using Fig 3.1, the pressure hysteresis can now be described qualitatively, as was done for the Schwarz-Khachaturyan theory in the last chapter. Near vacuum, the metal hydride is composed of purely the α phase. As the pressure of hydrogen gas is increased, the chemical potential of the gas, μ_g, also increases. Let c_α^{abs} and c_β^{abs} be the compositions of the α and β phases at the absorption plateau with c_α^{des} and c_β^{des} the values for the desorption plateau. Then, during absorption, only α phase can exist in the regime of $\mu_g < \mu_\alpha(c_\alpha^{abs}) = \mu_{2ph,abs}$. However, note that as seen in Fig 3.1, $\mu_\beta\left(c_\beta^{des}\right) < \mu_\alpha(c_\alpha^{abs})$. The system may be in either phase in the regime $\mu_\beta\left(c_\beta^{des}\right) < \mu_g < \mu_\alpha(c_\alpha^{abs})$, but since the system is undergoing absorption, no β phase has formed yet. The chemical potential is not yet high enough to compensate for the formation of dislocations as the β phase forms. Then, at $\mu_g = \mu_\alpha(c_\alpha^{abs})$, the chemical potential is now high enough to begin the phase

transformation and produce the necessary dislocations for β phase formation. In accordance with typical phase transformation theory, as α phase transforms to β phase, the absorption pressure is predicted to be constant. Then, once the transformation is complete, there is pure β phase. Additional increases in pressure result in increases in the number of interstitial hydrogen atoms in the β phase. This same reasoning may be applied in reverse for the desorption transformation.

Once again, just as was done for Schwarz-Khachaturyan Theory, consider the difference of the chemical potentials to arrive at the size of the hysteresis gap:

$$\begin{aligned}\mu_{2ph,abs}(\bar{c}) - \mu_{2ph,des}(\bar{c}) &= \frac{1}{c_\beta - c_\alpha}\left(g_{chem,\beta}(c_\beta) - g_{chem,\alpha}(c_\alpha) + \Delta h_{disl}\right) \\ &\quad - \frac{1}{c_\beta - c_\alpha}\left(g_{chem,\beta}(c_\beta) - g_{chem,\alpha}(c_\alpha) - \Delta h_{disl}\right) \\ &= \frac{2\Delta h_{disl}}{c_\beta - c_\alpha} \end{aligned} \tag{3.7}$$

As used in the previous chapter, the pressure of hydrogen gas is directly related to its chemical potential:

$$\mu_g = \mu_g^0 + \frac{1}{2}kT\ln\left(\frac{p_g}{p_g^0}\right)$$

where μ_g^0 and p_g^0 are the chemical potential and pressure at some reference state, p_g the pressure of the gas and μ_g its corresponding chemical potential. In the absorption two-phase region, due to equilibrium, $\mu_g = \mu_{2ph,abs}(\bar{c})$, while in the desorption two-phase region, $\mu_g = \mu_{2ph,des}(\bar{c})$. Hence,

$$\begin{aligned}\frac{1}{2}kT\ln\left(\frac{p_g^{abs}}{p_g^{des}}\right) = \mu_{2ph,abs}(\bar{c}) - \mu_{2ph,des}(\bar{c}) &= \frac{2\Delta h_{disl}}{c_\beta - c_\alpha} \\ \ln\left(\frac{p_g^{abs}}{p_g^{des}}\right) &= \frac{4\Delta h_{disl}}{kT\left(c_\beta - c_\alpha\right)} \end{aligned} \tag{3.8}$$

where p_g^{abs} is the absorption plateau pressure in the two-phase region and p_g^{des} is the desorption plateau pressure.

3.4 Beyond Flanagan-Clewley theory

Just like Schwarz-Khachaturyan theory, Flanagan-Clewley theory also makes some simplifying assumptions. They are fewer in number, but they may have a much larger impact on the predictions of the theory when considered more rigorously.

For example, one potential term worth reconsidering more carefully is the intensive enthalpy of dislocation production, Δh_{disl}. The theory assumes this term is a constant with respect to $\bar{c}$ in order to derive the hysteresis in the manner mentioned earlier. However, Δh_{disl} has a very complex relationship with $\bar{c}$. Δh_{disl} is known to change in materials with the creation of dislocations. As dislocations are added to a material, the dislocation density rises, and it becomes less favorable for additional dislocations to be created. This phenomenon is due to the stress fields of the dislocations. These stress fields are proportional to $\frac{1}{r}$ from the center of the dislocation, and serve to attract or repel dislocations depending on their direction [3]. With an increase in dislocation density, these stress fields populate the material more densely, making it harder to add new dislocations because the energy to form the dislocation now also includes the energy to overcome these stress fields. This is a common feature of plastic deformation in several materials, and is known as work hardening. The more a material is plastically deformed, the more dislocations form and eventually prevent other dislocations from forming. This behavior serves to strengthen the material. For example, the yield strength of the material is now much higher than it used to be because it takes more energy to form dislocations in the material populated by dislocation stress fields than in the pristine material. Flanagan and Clewley report that the dislocation densities after the absorption phase transformation and the desorption phase transformation are both very high at 10^{11}-10^{12} cm^{-1}, similar to materials that have been cold worked to the point of significant work hardening [1]. In these dislocation density regimes, the energy required to form a dislocation is much higher than in a dislocation-free material. In order for Δh_{disl} to be constant throughout the phase transformation, the dislocation density needs to be constant as new β phase is formed. However, this has not been observed in practice. Dislocation studies show that the dislocation density actually increases throughout the transformation, for both absorption and desorption [1,4]. Hence, this

behavior can only be accommodated by a perceptible change in Δh_{disl}. This change is not directly related to $\bar{c}$ due to its directionality and phase dependence. During the absorption phase transformation, dislocations are primarily produced in β phase, whereas in desorption they are created in the α phase. It is also hard to remove dislocation once they have formed, lending a degree of irreversibility to the transformations. So, it might be better to conceptualize Δh_{disl} as a function of dislocation density, ρ, not $\bar{c}$, and the total Gibbs free energy in the two-phase region is now a function of ρ. The effect of this contribution can now be seen in the hysteresis gap itself, which becomes dependent on ρ, and is thus predicted to grow with Δh_{disl} as the transformation proceeds. This may be seen in the chemical potential curve as a slight upward motion in the two-phase region chemical potentials during absorption and a corresponding downward motion during desorption, as summarized in Fig 3.2. This slow uptick behavior during the phase transformation has been observed experimentally for metal hydride isotherms (Ch 7, 8).

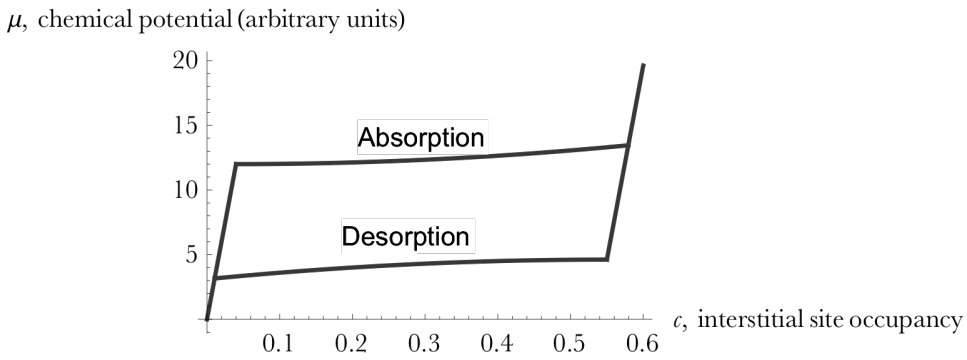

Fig 3.2. Chemical potential of metal hydride system predicted by the Flanagan-Clewley theory with work hardening. Compare this trend with Fig 2.1 for the Schwarz-Khachaturyan Theory and Fig 3.1 for the original Flanagan-Clewley theory prediction.

Finally, it is also unrealistic to ignore the strains that are being caused by misfitting hydrogen atoms in interstitial sites, especially when the free hydrogen atom is larger than the empty interstitial site in most materials. These strains add an additional element to the hysteresis, as discussed by Schwarz-Khachaturyan theory. In order to reconcile the effects

of both dislocations and misfitting strain, and provide a better picture of hysteresis, a combined general theory is necessary.

3.5 Chapter References

1. Flanagan, T. & Clewley, J. Hysteresis in metal hydrides. *Journal of the Less Common Metals.* 83, 127-141 (1982).
2. Conway, B. & Jerkiewicz, G. *Proceedings of the Symposium on Electrochemistry and Materials Science of Cathodic Hydrogen Absorption and Adsorption*. 17-26 (Electrochemical Society, 1995).
3. Dieter, G. *Mechanical metallurgy*. 171 (McGraw-Hill Book Company, 1961).
4. Flanagan, T. & Kishimoto, S. Hydrogen Traps in Cold-Worked Palladium. *Electronic Structure and Properties of Hydrogen in Metals* 623-628 (1983). doi:10.1007/978-1-4684-7630-9_87

Chapter IV

Experimental Setup and Procedures for In Situ X-ray Diffraction

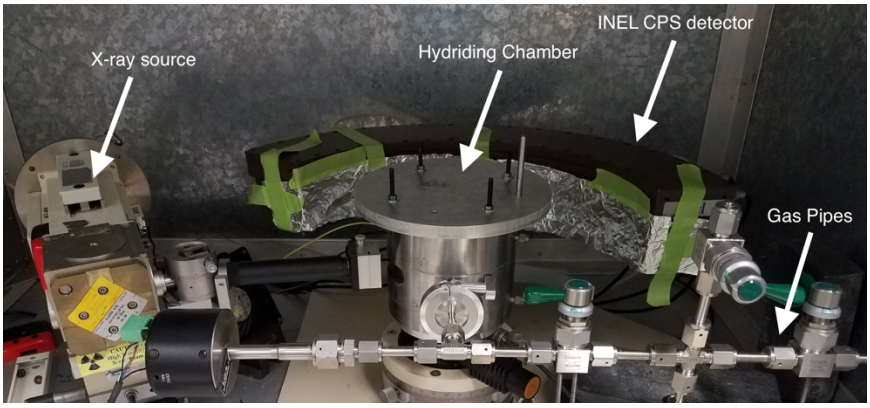

Fig 4.1. In-situ x-ray diffraction setup inside the x-ray enclosure.

The in-situ x-ray diffraction was performed in a customized diffraction and hydriding setup, within a metallic enclosure. The interior of the enclosure is shown in Fig 4.1. The detector is a Curved Position Sensitive 120° (CPS 120) detector from Instrument Electronique (INEL). The detector is covered with a few layers of aluminum foil to increase the signal-to-noise ratio for the counts measured by the detector. The aluminum foil is an effective attenuator of low-energy xrays.

The hydriding chamber is custom made, with an aluminum structure and a special beryllium window for entry of X-rays. There is a removable lid on the top to mount the diffraction sample. There is also another opening in the front, connected to gas pipes for introducing hydrogen into the chamber. Pressure gauges are connected to the gas pipes to monitor the pressure in the hydriding chamber and in the different parts of the pipes. These gas pipes are in turn connected to argon (Ar) and H_2 gas cylinders, and a vacuum pump. The Ar is present for purging the chamber before measurements are made in a pure hydrogen atmosphere. The vacuum pump is present to facilitate reducing the pressure in the chamber, as is the case during desorption measurements. The hydriding chamber also contains an internal resistive heating element with a connected thermocouple. The heating element

enables the diffraction sample to be kept at different temperatures. Throughout the measurements in this study, the heating has been set to ensure the temperature stays constant around 60°C. This temperature has been chosen because of its common use in previous studies on Pd [1, 2]. Using the same temperature as these other studies facilitates easy comparisons to their data.

Finally, the x-ray source consists of a molybdenum (Mo) target. Mo was chosen for its high $K\alpha_1$ energy, 17.5 keV, one of the highest energies commonly used in lab diffractometers [3]. From Bragg's law, a high diffraction energy corresponds to a small diffraction wavelength, which in turn results in peaks that occur at lower values of θ. Hence, more peaks can be acquired within the available angular detection range of the detector. The X-rays are generated using the Rigaku Gigerflex x-ray high voltage generator (not shown in Fig 4.1), set to a current of 50mA at a voltage of 45kV.

Diffraction measurements are typically acquired until any peak in the profile measured by the detector reaches 2500 counts. This acquisition typically takes 15-20 minutes for bulk materials of a single phase.

The Pd used in this study was a 200-mesh powder of 99.95% purity acquired from Alfa Aesar. Prior to any diffraction profiles were measured, the material was annealed at 1000°C to ensure that it would be defect-free before cycling. This procedure enables the isolation and analysis of defect production due to the hydride cycling itself.

4.1 Cycling Procedure and Measurements

A single full hydriding cycle of Pd is done by the following procedure: first, the Pd is placed into the chamber which is pumped to vacuum and purged a few times with Argon to ensure that almost no atmospheric air remains in the chamber. Then, a diffraction profile is measured at vacuum. Using the gas manifold, hydrogen gas is then introduced into the chamber at intervals of approximately 10-15 torr initially. For each interval, once the desired initial pressure is reached, the system is allowed to come to equilibrium for 2 hours. After this period, diffraction profiles are acquired, and the pressure is increased again. This procedure ensures that the data acquired can be analyzed in conjunction with thermodynamic theories, which only apply at equilibrium conditions. Once a pressure of about 80 torr is reached, the

intervals are changed to 2-3 torr because the absorption plateau for Pd at 60°C is near. Once the plateau is over, which is determined by the presence of just one phase in the diffraction profiles, the intervals between measurements are changed to 50-100 torr, until a pressure above 500 torr is reached. This concludes the absorption portion of the cycle, and the desorption portion begins. With the vacuum pump, the pressure in the chamber is reduced in intervals of 40-50 torr until a pressure of 50 torr is reached. Then, the intervals are once again changed to 2-3 torr because the desorption plateau for Pd at 60°C is near. The desorption is carried out in this way until vacuum is reached, and a final vacuum diffraction measurement is conducted.

The Pd powder has been cycled up to two consecutive times, to observe changes in defect density over the course of more than one cycle. A "minor loop" has also been carried out. In a minor loop, the pressure is increased during absorption and diffraction profiles are acquired until a point in the absorption two phase region where about 70% of the phase transformation is complete, as determined by phase fractions from analysis of the diffraction profiles. Then the desorption is started and followed in the same manner as for the full cycle. The minor loop aids in the analysis of effects that may be occurring over the course of an entire absorption or desorption plateau. The minor loop causes these effects to be stopped before they reach the level they reach in the entire cycle. Hence, the magnitude of these effects, and their change over the course of a cycle, may be estimated.

4.2 Analysis Procedures

The resulting diffraction profiles and pressure measurements from every cycle are tabulated and investigated with diffraction refinement techniques and hydrogen uptake analyses. The hydrogen uptake analyses are based on using the recorded pressure changes to achieve equilibrium over the course of the two hours of equilibration time before every diffraction profile measurement. These pressure changes are related to the uptake of hydrogen gas by the material, and therefore, the increase in hydrogen concentration in the material with every increase in pressure. In particular, pressure-concentration isotherms can be generated. The isotherms were generated by using the REFPROP program created by NIST, which provides a hydrogen gas equation of state that can be used in conjunction with

the measured relative differences in pressures to estimate concentrations. The pressure-concentration isotherms are important analysis tools because they provide an insight into the chemical potentials, as discussed in Ch 2 and 3, and the concentration values provide a useful axis to visualize and gain insights from other datasets generate from the X-ray diffraction profiles, such as the lattice parameter, phase fraction and strain.

The diffraction refinement techniques used to analyze the X-ray profiles, and derive datasets such as the lattice parameter, phase fraction and strain, are discussed in the next two chapters, Ch 5 and 6.

4.3 Chapter References

1. Syrenova, S. et al. Hydride formation thermodynamics and hysteresis in individual Pd nanocrystals with different size and shape. *Nature Materials* 14, 1236-1244 (2015).
2. Flanagan, T. & Clewley, J. Hysteresis in metal hydrides. *Journal of the Less Common Metals.* 83, 127-141 (1982).
3. Fultz, B. & Howe, J. *Transmission electron microscopy and diffractometry of materials*. 17-18 (Springer, 2013).

Chapter V

Detector Complications and Machine Learning for Feature Extraction

One of the idiosyncrasies of the raw diffraction profile data acquired from the INEL CPS detector has been the presence of "shoulder peaks", always trailing the main peaks and consistently around 20% to 30% of the height of the main peaks they trail. The form of this peculiar behavior is shown in Fig 5.1:

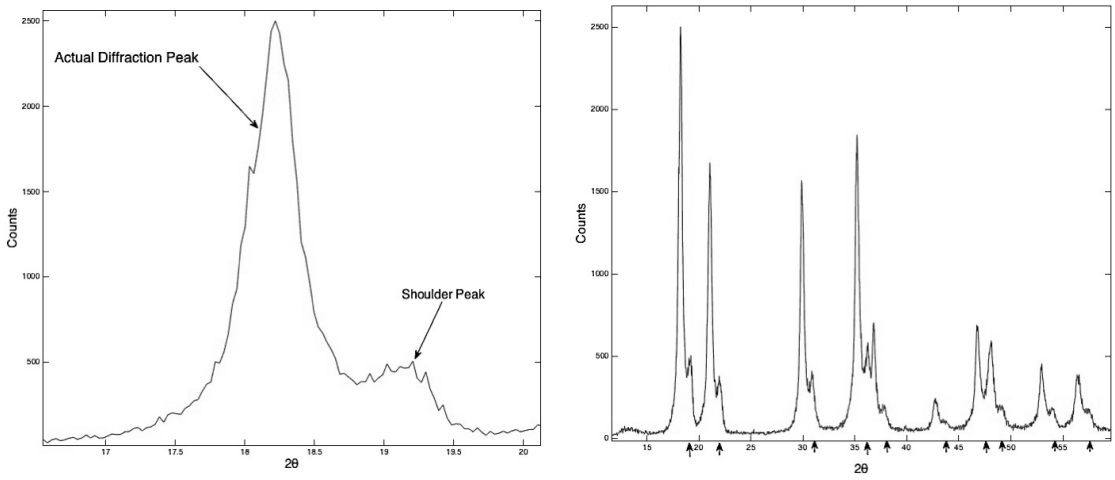

Fig 5.1. The shoulder peaks found in the raw data from the INEL CPS detector. The graph on the left is a view of just one peak, the (111) diffraction for Pd, and its associated shoulder. The graph on the right is a complete raw diffraction profile for Pd, with the locations of shoulder peaks marked by arrows along the horizontal axis.

5.1 Origin of Shoulder Peaks

These "shoulder peaks" are an artifact of the INEL instrument itself, likely due to the aging of the detector and its associated electronics, as they were initially acquired nearly three decades ago. A schematic of the signal processing workflow from the INEL's count measurements to the calculation of the diffraction profile is given below.

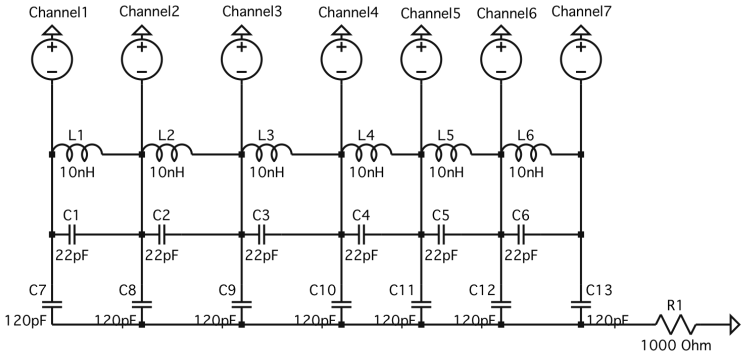

Fig 5.2. Schematic of a small segment of the delay line circuit, with just seven channels. The real delay line has 4096 channels, but has the same repeated circuitry as in this schematic. The capacitors may be especially prone to change in behavior over time.

The detector contains arrays of capacitors and inductors in series, known as delay lines, as seen in Fig 5.2. In short, this circuit enables the spatial signal collected by the CPS to be converted into a temporal signal. As their name suggests, the delay lines 'delay' the signal collected by each of the individual channel detectors in the CPS by a known amount, depending on where they are located along the circuit. This enables the counts collected spatially by the detector to be read into the INEL's data collection instruments as a current signal varying temporally. It is this analog current signal that is then converted to the raw diffraction profile stored in the INEL's digital memory buffers. The delay line circuit has several small electronic parts. It is necessary for all of these parts to be working correctly in order for the signal to be correctly converted to count values in the INEL's memory buffers. However, it is well known that capacitors, especially ceramic ones, tend to lose capacitance over time. The mechanism of this change is as follows: perovskite materials like $BaTiO_3$ are commonly employed as the dielectric material in ceramic capacitors. At a microscopic level, they contain magnetic domains. When the capacitors are first fabricated, these domains are arranged in completely randomized directions, but over time, due to the thermal energy of the individual atoms, the domains gradually change to a non-random energetically favorable configuration that reduces the overall polarization density, and consequently the dielectric constant of the material. The lowered dielectric constant directly leads to a lower capacitance for the entire capacitor. Circuit simulations have been conducted on the delay lines, using

SPICE (Simulation Program with Integrated Circuit Emphasis), a commonly used circuit simulation program. The simulated circuit has been built according to the specifications for the delay lines found in the detector's documentation. It has been found that a reduction in the capacitance of some of the delay lines capacitors may lead to a change in the temporal signal transported to INEL's electronics, and this change could potentially manifest itself as the shoulder peak. In particular, a circuit with just 7 detector channels was constructed, as seen in Fig. 5.2. The channels were set so that a 'peak' would be simulated in channel three with a voltage pulse 3 seconds long, consisting of maximum voltage of 20V held for 1 second, another second to ramp up to this value and a final second to ramp down. Then the capacitor C9's capacitance was lowered by 50% to 60pF. The resulting current through the end of the delay line at R1 was measured over time for the 3 seconds of the voltage pulse. The reduction of capacitance of just C9 led to an increase in the current after the main pulse, similar to the "shoulder peaks", as seen below.

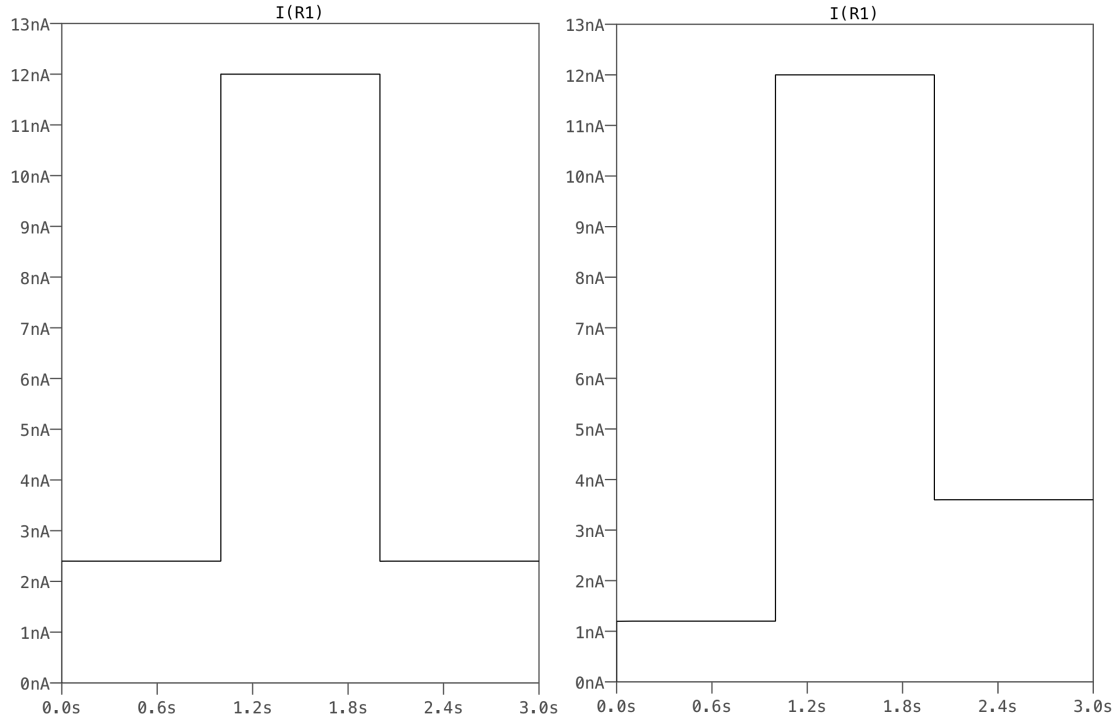

Fig 5.3. The simulated current leaving the delay line circuit. The graph on the left is the ideal case with all the components functioning as per their specifications in the documentation and Fig 5.2. The graph on the right is the case when one of the capacitors, C9 in Fig 5.2, has lost 50% of its capacitance.

There are 4096 channels in the CPS detector, so it is very probable that some of the circuit components have had a change in behavior over the past three decades, leading to the "shoulder peaks". These peaks are an important consideration in the analysis of the ensuing diffraction data, for a variety of reasons. They substantially reduce the ability of common diffraction profile analysis techniques like Rietveld refinement to obtain accurate values for lattice parameters, peak broadenings and other materials properties. Obtaining accurate instrumental broadening parameters for the detector using a diffraction profile from a standard material (Eg. LaB_6 or Si) cluttered with these shoulders is a very difficult and nearly impossible task. Finally, understanding phase transitions is the major thrust of this research, and phase transition regimes often have peaks from two or more different phases in close proximity. It is already a difficult task to reliably and rigorously fit diffraction profiles with nearly overlapping peaks of different phases. The presence of shoulders which often overlap and change the effective amplitudes of the peaks of different phases further complicates this problem. Hence it is necessary to develop techniques to convert the shoulder-filled raw data of the INEL detector into shoulder-free diffraction profiles well suited for techniques like Rietveld refinement.

5.2 Manual fitting and subtraction of shoulder peaks

Studies have been done on the various characteristics of the shoulder peaks relative to the preceding actual diffraction peak. The behavior of the amplitudes and locations of the shoulder peaks are typically as shown in Fig 5.4. The data in the figure was calculated for a single raw x-ray diffraction profile of silicon. However, these same trends persist in the diffraction profiles of other materials collected from the INEL detector.

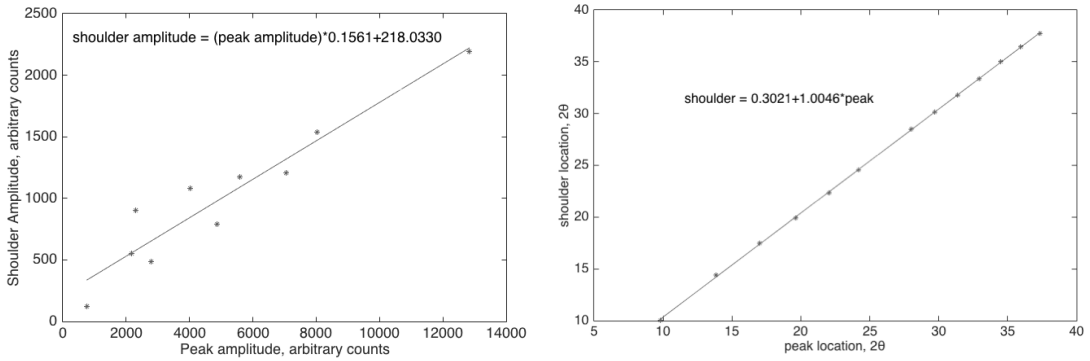

Fig 5.4. Trends in amplitude and position for the shoulders for the diffraction profile of silicon. The graph on the left is for the amplitudes and the graph on the right is for peak positions. There are clear linear trends present in both cases.

The clear linear trends in Fig 5.4 suggest that the shoulder is a very repeatable and predictable feature of the data. Hence, it is possible to remove it by understanding these basic trends and behaviors. To accomplish this removal manually, the peaks and shoulders in a raw diffraction profile are fitted individually with Voigt profiles and a cubic background to capture as much of the variation in the dataset as possible. Then the Voigt terms corresponding to shoulder peaks are dropped to arrive at a new, altered profile devoid of shoulders and suitable for typical profile refinement techniques. This fitting was carried out using the multi-peak fitting package of Igor Pro. Fig 5.5 summarizes this technique, as carried out on the first few peaks of the diffraction profile of Pd.

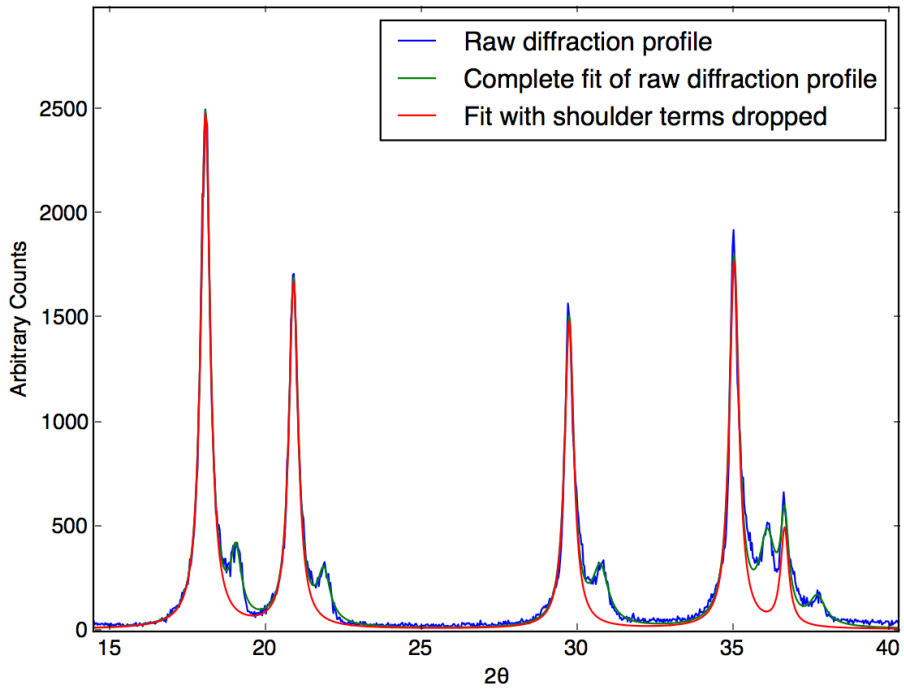

Fig 5.5. Manual fitting and removal of the shoulder peaks. Each real peak and shoulder is fitted with a Voigt function, with a cubic background.

The primary advantage of manually removing the shoulder peaks is that it can be done with high precision – all the shoulder peaks will disappear completely because they are fitted individually. However, there are two major disadvantages that detract from the practical usability of this technique. Firstly, it is a very time-consuming method – precise fitting for just a handful of peaks can take at least 10 minutes for each fitted profile. In this project, this can lead to several hours of fitting for just one hydrogen cycling dataset, which may consist of 60 or more diffraction profiles. Secondly, some shoulders are very hard to remove due to their small size or overlap with other peaks. Diffraction peaks that occur at high angles, in the range of $2\theta > 40°$, are of interest to correct for sample alignment effects from the experimental setup. But, these peaks tend to have low amplitudes due to the Debye-Waller factor, and consequently the shoulders are also hard to differentiate, distorting the actual peaks. More importantly, as mentioned earlier, when two phases exist and the diffraction peaks of each are close, shoulders are a significant problem. In these conditions, it

is impossible to accurately fit the shoulders individually and manually. Hence, an efficient, automated technique that can detect and remove all shoulders is still required.

5.3 Machine learning for automated shoulder removal

The several strong trends present in the shoulder peaks' characteristics suggest that they could be modeled with machine learning techniques. The problem of removing them from the diffraction profiles can be formulated as a machine learning regression question: what is the value of the count correction that must be subtracted from any given detector channel's count number to arrive at a shoulder-free diffraction profile? A machine learning model was built and trained to answer this question. Gradient Boosting with Decision Trees (GBDT) was chosen to be the algorithm to create the model. A decision tree is a set of if-then-else decision rules to describe the behavior of the data [1]. Gradient boosting is what is known as an ensemble learning technique: a method that combines several models to produce a resultant model that is able to describe the data better than any of the constitutive models. In particular, gradient boosting is the term for ensemble learning when the constitutive models are trained sequentially on the residuals of the previously trained constitutive models. For example, constitutive model 1 is trained on the original data, then constitutive model 2 is trained on the residuals of model 1, model 3 on the residuals of combined model 1 & 2, and so on. Decision trees are often used as the constitutive models for gradient boosting because they are very computationally fast: the time complexity of predicting with a decision tree is logarithmic in the number of data points used to train it. Gradient boosting itself is considered to be one of the most effective of all ensemble learning techniques [1]. For this particular regression problem of correcting shoulder peaks, GBDTs were used due to their effectiveness in practical machine learning problems. They are a well-researched technique known for their predictive power and robustness to outliers and overfitting, both of which are important considerations for the x-ray diffraction data: since the x-rays originate from a molybdenum source, and not a synchrotron, they naturally have more of an angular and spectral spread, which leads to noise in the diffraction profiles acquired.

To allow for the GBDT model to be effectively used with a variety of diffraction profiles, the model was trained on a specially collected data set that primarily captured the anomalous shoulder behavior of the detector, while minimizing any effects of the identity of the sample used for diffraction. Amorphous GeO_2 was used as the sample to ensure that the diffraction data did not have any significant Bragg diffraction peaks. Furthermore, to understand the potential variation of the shoulder with channel number on the detector, lead slits were used. Lead sheets were used to cover most of the detector except for a single slit that allowed x-rays diffracted from the sample to reach the detector channels. Diffraction profiles of the GeO_2 were taken in this manner, at 22 different positions of the slit, about equally spaced across the 2θ range from 0° to 60°, the range used for most diffraction profile refinement analysis. A typical lead slit GeO_2 diffraction profile is given below:

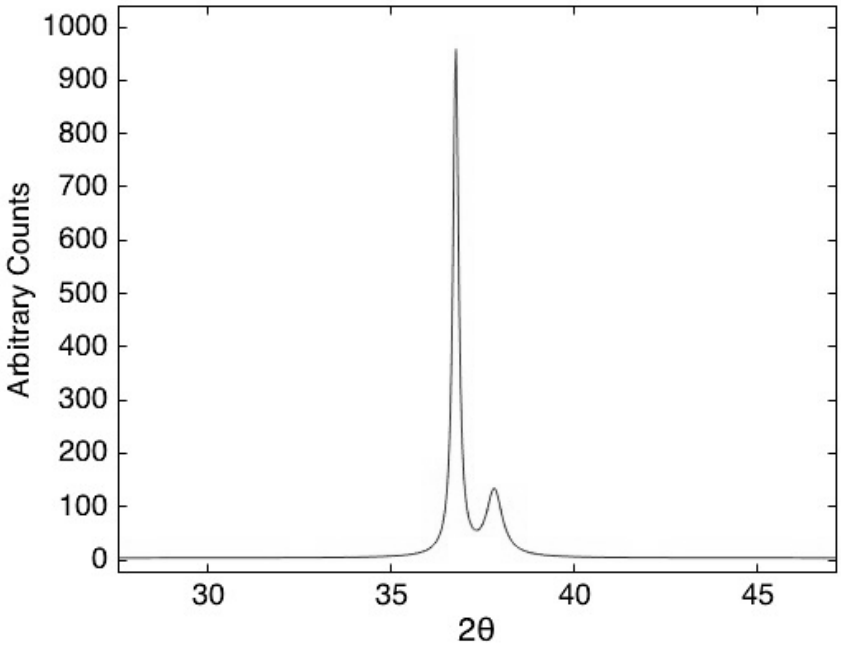

Fig 5.6. An amorphous GeO_2 diffraction profile with the detector covered by a lead slit. The shoulder peak is clearly visible to the right of the main peak at the location of the slit.

The 22 different diffraction profiles collected in this manner were then fitted in Igor Pro with Voigt peaks as outlined in the previous section. Then, the terms corresponding to

shoulders were computed and stored separately, to be used as the training outputs of the model.

Sci-kit learn, the well-known python package for machine learning [2], was used to create the GBDT model, and the code used is given in Appendix A. It was assumed that the shoulder's effect on the counts of any given channel would be a function of the number of counts in preceding channels. This follows from the fact that the shoulder peak itself is believed to be a nonlinear function of the preceding actual peak due to the electrical components of the detector. Hence, the input regressors for the model consisted of several counts of channel preceding the channel for which the shoulder excess was being predicted. The input regressors also included the number of the channel being estimated, from 0 to 4095. The exact number of preceding counts in the input regressors was left as a hyper-parameter to be determined by trial and error. A random scaling was employed: every raw profile would be scaled by a multiplicative factor between 0 to 10. This ensured that the height of the background relative to the peaks, a factor that varies with the amount of time data is collected in the detector, would not adversely affect the generalizability of the model to future diffraction profile from a varied set of materials and data collection times.

Once the data from the individual channels of the 22 diffraction profiles was processed in the manner outlined above, GBDTs were built on the data with the number of decision trees employed and the maximum depth of each of the trees as hyperparameters. Through a grid search, it was found that models with 500 decision trees of maximum depth 5, and the counts of 100 previous channels to predict the shoulder effect on the current channel, provided the best combination of hyperparameters for the model to work effectively on real diffraction patterns for several materials, like Si, LaB_6 and Pd. This model has been applied to a variety of diffraction profiles produced by the INEL detector and has been observed to be very effective in removing shoulder peaks. The typical shoulder removal is shown in the superimposed profiles below:

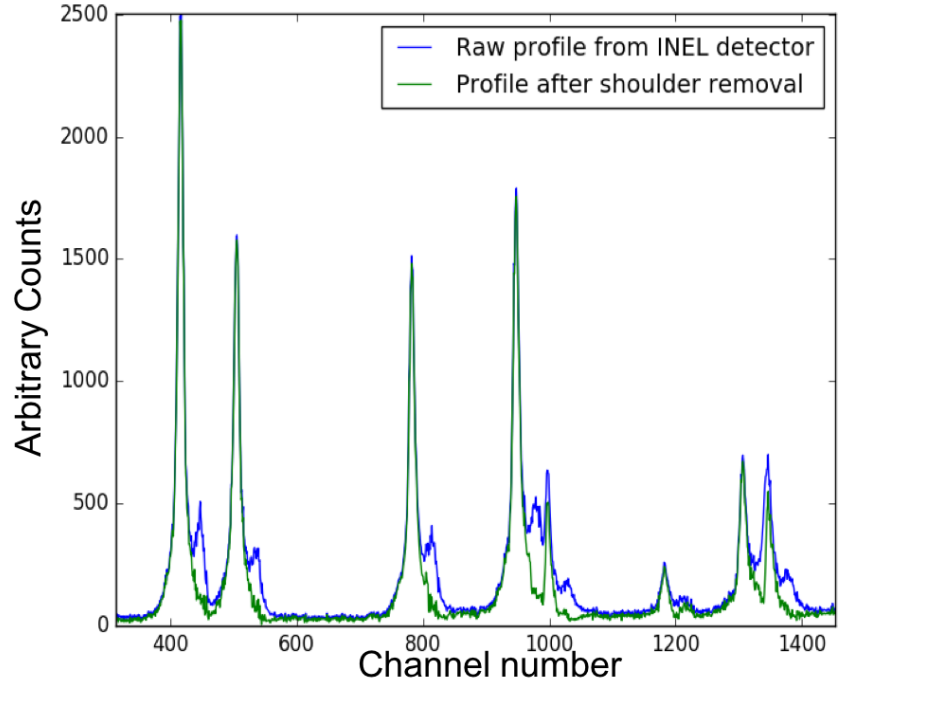

Fig 5.7. Shoulder removal with machine learning for a Pd diffraction profile. The model is able to account for the shoulder even when actual peaks are relatively close.

The time required to predict the shoulder-free profiles from the raw profiles of the detector is less than a second, making this technique a very fast way to remove shoulders, antithetical to the manual fitting mentioned before, which would at least take 10 minutes per a profile. Furthermore, as Fig 5.7 reveals, even the shoulders of small peaks and very close peaks can be properly accounted for. The removal of the shoulder in Fig 5.7 may not appear to be significantly different from Fig 5.5, but it is much more robust when there is more than one phase present, as occurs during the phase transformation of PdH in this work. As seen below, the machine learning model is once again very effective even in the two-phase regime:

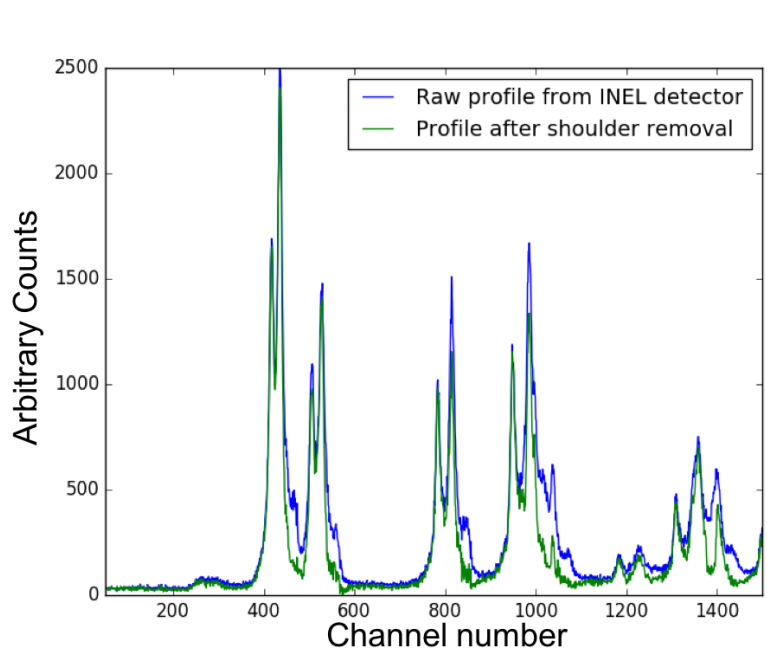

Fig 5.8. Diffraction profile in the 2-phase region of the PdH α to β phase transition, with the machine learning model applied to remove shoulders. The intensities of some of the raw peaks are observed to be reduced because their heights have been exaggerated by overlap with the shoulders of other peaks.

Hence, this technique is effective to meet all of the purposes outlined earlier in the chapter: allowing for profile refinement, determining reasonable peak broadenings (for instrument parameters, size and strain effects), and measuring phase transitions accurately. From this point, all profiles shown and refinement analyses conducted are of data from the INEL detector that has already been preprocessed with the machine learning GBDT model.

5.4 Chapter References

1. Chen, T. & Guestrin, C. XGBoost. *Proceedings of the 22nd ACM SIGKDD International Conference on Knowledge Discovery and Data Mining - KDD '16* (2016). doi:10.1145/2939672.2939785

2. Varoquaux, G. et al. Scikit-learn. *GetMobile: Mobile Computing and Communications* 19, 29-33 (2015).

Chapter VI

Sequential Refinement of Diffraction Profiles

The analysis of the x-ray diffraction profiles in this work is focused on understanding materials properties that can be determined from the trends present in the profiles. These properties primarily include lattice parameters, strains, and phase fractions. They may be acquired in a robust and well-studied manner through the employment of diffraction profile refinement techniques, such as the Rietveld and Pawley methods. GSAS-II, a software developed by the Argonne National Laboratory, has been exclusively used for the refinement, for a couple of reasons. It has the needed features suited to the experimental setup of this project, including the special properties of the Debye-Scherer diffraction setup, and an efficient routine for sequential refinement of several diffraction profiles. In addition, it is open source and implemented in the Python programming language, making it very easy to add custom features unique to an experiment.

The well-known Rietveld refinement method was used almost exclusively to analyze diffraction profiles. Some trials have also been done with Pawley refinement, a technique similar to the Rietveld, which considers individual peak intensities to be free parameters during fitting. However, the Pawley technique has led to fitting solutions that are not very well behaved for all the sequential x-ray diffraction profiles. The Rietveld method has offered more repeatability and better fitting.

6.1 Material Parameters from diffraction refinement

An important factor in analyzing phase transitions with x-ray diffraction is understanding the extent of the transitions during the acquisition of each diffraction profile. Phase fractions, which measure the extent of the transitions, are determined by integrating the areas of the peaks of each phase and normalizing these areas to produce fractions. Another important factor are the trends in the lattice parameter, which are determined from diffraction profiles using peak positions. From Bragg's law, it is well

known that the peak positions are related to the spacing between different planes in a crystal lattice, which are in turn all dependent on the lattice parameter. However, to just naively utilize Bragg's law to determine lattice parameters, the x-ray beam must be of negligible angular and spectral spread, and the sample being measured must be positioned directly at the center of the detector's circular arc. Any deviations from these assumptions will result in deviations from the ideal scenario of Bragg's law, and corrections must be introduced in line with the characteristics of the experimental setup in use. In the case of the INEL CPS detector, these corrections have been calculated and tabulated, and these methods are incorporated in this work to allow for more precise lattice parameter determinations [1].

A final parameter of special interest is the strain of crystals during the phase transition. During the phase transition, the transforming phase can constrain the forming phase, as discussed in Ch 2. In addition, the misfitting hydrogen interstitial cause distortions of the lattice, as seen in Ch 2. Both of these effects lead to strain in the material. The effects of the strains may be seen in the lattice parameter, which has some small variation within a single phase of the material, leading to peak broadening [2]. In GSAS-II, 'microstrain' is calculated and this refers to 10^6 times the strain. This terminology is also used later in the study, because it provides a useful scaling for visualizing the strain.

6.2 Instrumental Contributions to Diffraction Profiles

Not all of the peak broadening can be attributed to the strain, as there is some level of intrinsic broadening due to the instrumentation itself. Hence, the broadening of an ideal material, with no intrinsic effects, is determined and factored into future measurements to account for the instrumental broadening. In this work, LaB_6 (NIST standard material 660b) was used to determine the instrumental broadening. LaB_6 has a simple cubic structure, allowing for it to have several peaks within a given 2θ range in its diffraction profile, leading to better accuracy in determining instrumental broadening parameters.

The instrument-specific contributions have been described with a variety of terms characterizing the different effects of the instrument on diffraction profiles. One of the most important of these terms is a 'zero' term, to capture a constant offset of the detector measurements in 2θ. Another important term is the ratio of $K\alpha_2$ to $K\alpha_1$ radiation. Since the source of x-rays is a molybdenum elemental target, the x-ray spectral distribution from the source is a bremsstrahlung, with peaks at locations corresponding to valence-to-core electronic transitions in the molybdenum atom. The highest energies of these transitions are the $K\alpha_2$ and $K\alpha_1$, with the $K\alpha_1$ being slightly higher. To ensure that the diffraction data is easier to analyze, the radiation from the source is limited to a narrow range of wavelengths near the $K\alpha_1$ using a monochromator. However, the wavelength selection is not always fine enough to purely encompass $K\alpha_1$, so some $K\alpha_2$ will also be present. From Bragg's law, it can be immediately observed that this will lead to some amount of peak splitting due to the differing wavelengths of radiation, but this is once again an artifact of the experimental setup. Hence, the ratio of $K\alpha_2$ to $K\alpha_1$ is also a part of the instrumental parameters. Then come the Caglioti fitting terms, which describe the broadening at the Full Width at Half Maximum (FWHM). In common diffraction peak fitting, the individual peaks are assumed to be a pseudo-Voigt function, a linear combination of a Gaussian and a Lorentzian peak. The Caglioti terms quantify the broadening of the Gaussian and Lorentzian peaks separately, with a dependence on θ. This approach allows the broadening of all peaks in a profile to be described with just 5 terms: U, V, W, X and Y, and is the most common method of accounting for instrumental broadening. Next, intensity reductions due to the potential polarization of the incident x-ray radiation on the sample are considered: the component of the polarization that is in the plane of the diffraction itself has its intensity reduced, whereas the component perpendicular to the plane is unaffected, and this behavior is quantified with a polarization parameter. This is a consideration for this lab diffraction setup because x-rays from elemental targets are unpolarized and contain both of these components. Finally, the Lorentz factor is fitted, which quantifies the statistical likelihood of a diffraction occurring, as not all the crystallites are perfectly oriented for complete diffraction of incoming radiation as specified by Bragg's law.

6.3 Refinement Procedure

When fitting data to a function with a multitude of terms, each having different effects on the fitting, it is common to fit increasingly large subsets of the terms, instead of fitting all terms at once, to ensure that the fitting solution moves more easily towards the global minimum of the fitting error space, as opposed to a local minimum. This holds true for diffraction profiles and Reitveld refinement. It is also a special focus in the case of sequential diffraction profile analysis to ensure that all of the profiles are fit satisfactorily. Here is a summary of the general fitting procedure for reproducible and efficient Rietveld refinement of the sequential diffraction profiles: First, set the initial values of the lattice parameters to the measured values of both phases in the pure state and the experimental conditions. Setting lattice parameters close to their actual values helps to ensure the fitting converges. Then, limit fitting to the 10°-50° range in 2θ. Diffraction peaks only start appearing after 10° in Pd. Fitting beyond 50° would include higher order peaks, but they are often not as resolved as the lower order peaks and are also of lower intensity, due to the Debye-Waller factor, atomic form factor and strains. Including these peaks leads to lower quality fits, and they do not provide any additional value due to their low resolution. Hence, they are safely excluded to improve the fitting of the rest of the peaks. Finally, before any fitting is done, add a constraint on the minimization: set the phase fractions to equal 1 on summation. Constraints help to ensure that the fit converges to a solution that describes the real experimental scenario, and in this case, the total phase fractions must equal one when added.

For the fitting, just one profile is initially refined, usually the very first diffraction profile that has been collected as part of the hydrogen uptake cycle. Hence, it is purely the initially present phase. First the lattice parameters and phase fractions are simultaneously refined, followed by a Chebyshev background function with 6 terms, and the strain broadening and detector sample displacements mentioned before.

To refine the remaining profiles, the background, strain and sample displacement terms from the first fit are used to initializes the corresponding values for the remaining profiles, and these values are not initially refined. Lattice parameters are also not initially

refined for the profiles: it has been found that refining lattice parameters too early can lead to a misattribution of peaks to different phases, especially in the two-phase region, as the fitting enters a local minimum that is far away from the global minimum. The lattice parameters remain as they were fit for the first profile. Only the phase fractions of the remaining profiles are allowed to be free parameters in the sequential fitting of the remaining profiles. This enables the fitting to correctly identify and attribute different peaks to different phases very early on. Once the phase fraction fitting shows that the peaks are correctly attributed in all profiles, the refinement of lattice parameters for all profiles can be started. Finally, the sample displacement, background terms and microstrain are added in subsequent refinements, to conclude the fitting. Through repeated usage, this procedure has been shown to be very reproducible and effective to ensure that all the profiles are fitted well, and create new datasets of lattice parameter, strain and phase fractions to reasonable accuracy to allow for analysis and interpretation.

An example of a profile fitted in this manner in GSAS-II is given in Fig. 6.1.

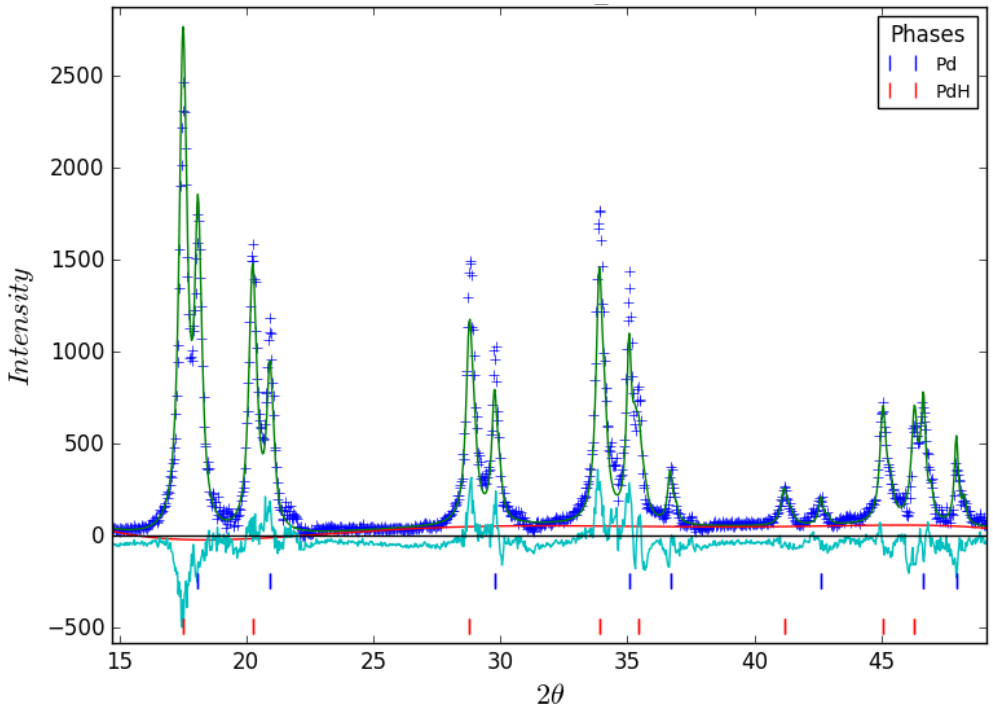

Fig 6.1. A diffraction profile from the two-phase region of the PdH system, fitted in GSAS-II. The blue '+' markers are the diffraction data, the green curve is the

complete fitting function, the red curve is the background and blue curve consists of the residuals of the fit.

6.4 Chapter References

1. Rowles, M. & Madsen, I. Whole-pattern profile fitting of powder diffraction data collected in parallel-beam flat-plate asymmetric reflection geometry. *Journal of Applied Crystallography* 43, 632-634 (2010).
2. Fultz, B. & Howe, J. *Transmission electron microscopy and diffractometry of materials*. 432-434 (Springer, 2013).

Chapter VII

Results of Diffraction Analyses, and Comparisons to Existing Theories

As shown in the previous chapter, diffraction profile fitting allows for the extraction of lattice parameters, phase fractions and strains in each phase to high enough accuracy to allow for an analysis of changes arising from hydrogen gas uptake. In addition, as outlined in Ch 4, the analysis of the pressures that were introduced into the chamber, and the resultant equilibrium pressures, allows for the calculation of absolute hydrogen uptake: the fraction of available interstitial sites that are occupied by hydrogen atoms, $\bar{c}$. When visualized with pressure, this data leads to pressure-concentration isotherms, which are a commonly used representation of hydrogen uptake properties and hysteresis for metal hydrides.

In the ensuing graphs of this section, unless otherwise stated, data from the second consecutive absorption-desorption cycle is used. The motivation for using the second, as opposed to first, is due to the nature of the initial material. As mentioned in Ch 4, the Pd powder was annealed, so it is assumed to be initially free of dislocations and other defects. However, the process of hydrogen uptake leads to strains, and the material after the first cycle will contain more defects in its microstructure than the precursor material. Cycling in metal hydrides, especially in Pd, is found to be a relatively reversible process, even with respect to the hysteresis. Flanagan and Clewley thus conclude that after the first cycle, subsequent cycles always return the defect density back to its original value at the start of the given cycle. It is only the first cycle that leads to a noticeable net increase in defect density from start to finish. Schwarz and Khachaturyan have a similar conclusion that defects being generated in the first cycle contribute more to the hysteresis than in subsequent cycles, owing to a large increase in dislocation density during the first cycle that leads to work hardening of the material. Hence, to control for the additional hysteresis component caused by the rapid increase in dislocation density during the first cycle, the second cycle is shown the most in the ensuing data. Additionally, the trends

related to the predictions of the Schwarz-Khachaturyan theory and Flanagan-Clewley theory found in additional collected data, such as the minor loop and other complete cycles, are mostly of the same form. The second cycle's data provides a broad summary of the trends related to the two theories in a comprehensive manner.

7.1 Pressure-concentration isotherms

The typical pressure-concentration isotherm measured for the palladium-hydride system using the in-situ x-ray diffractometer setup is shown below:

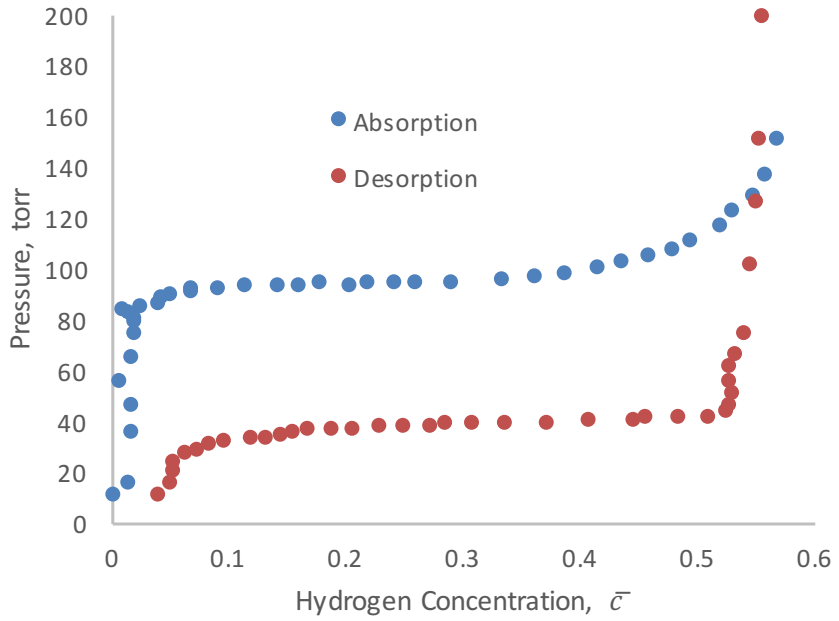

Fig 7.1. Palladium hydride pressure-concentration isotherm during its second cycle measured in the in-situ x-ray diffractometer.

The absorption pressure is around 93 torr for absorption and 37 torr for desorption. These values are from the pressures found at the middle of the phase transformation (equal amounts of both phases). As seen in Ch 2, the Schwarz-Khachaturyan theory gives a predicted gap of:

$$\ln\left(\frac{p_{g,SK}^{abs}}{p_{g,SK}^{des}}\right) = 8v_0 G_s \frac{1+\sigma}{1-\sigma}\frac{\left(c_\beta^* - c_\alpha^*\right)}{kT}$$

According to Syrenova and others, who perform calculations using the Schwarz-Khachaturyan theory for Pd at 60°C, conditions similar to this work, $\sigma = 0.39$, $v_0 = 0.273\text{Å}$, $G_s = 43.5GPa$ and $\varepsilon_0 = 0.035$ [1]. Observe from Fig 7.1, that $\left(c_\beta^* - c_\alpha^*\right) \approx 0.5$, which is the concentration difference between the phases at chemical equilibrium. With these values, it can be obtained that $\ln\left(\frac{p_{g,SK}^{abs}}{p_{g,SK}^{des}}\right) \approx 2.6$. The observed gap is:

$$\ln\left(\frac{p_{g,obs}^{abs}}{p_{g,obs}^{des}}\right) = \ln\left(\frac{93\ torr}{37\ torr}\right) = 0.92$$

The observed and predicted sizes of the hysteresis gaps are not close, but are of the same magnitude. The difference between the observation and the prediction may be explained through the myriad assumptions used to arrive at the final analytical expression for the hysteresis gap that may not hold in a true PdH system. For example, the transformation may not be completely coherent. Transmission electron microscopy (TEM) studies of the hydride phase transformation have shown that new phases form as precipitates that can vary between coherent and incoherent interfaces [2]. Additionally, as outlined in the beginning of Ch 2, the transformation from α to β phase in the palladium hydride system may consist of semi-coherent interfaces due to the lattice parameter difference from 3.89Å to 4.04Å. As presented in Ch 2, the more incoherent the interface becomes, the more the magnitude of the hysteresis gap is reduced compared to the prediction of the hysteresis equation derived by Schwarz and Khachaturyan. A more detailed analysis of these effects is presented in the next chapter.

Compared to the Flanagan-Clewley theory, the data bares less similarity. As seen in Ch 3, the Flanagan-Clewley theory predicts a hysteresis gap of:

$$\ln\left(\frac{p_{g,FC}^{abs}}{p_{g,FC}^{des}}\right) = \frac{4\Delta h_{disl}}{kT(c_\beta - c_\alpha)}$$

The stored energy from the cold working is on the order of magnitude of 0.1 meV per atom [3], and this value is related to the enthalpy of dislocation formation Δh_{disl}. Again using $\left(c_\beta^* - c_\alpha^*\right) \approx 0.5$ at a temperature of 60°C, the Flanagan-Clewley theory predicts a hysteresis gap of $\ln\left(\frac{p_{g,FC}^{abs}}{p_{g,FC}^{des}}\right) \approx 0.03$, an order of magnitude lower than the 0.92

observed. This suggests that the hysteresis effect is much larger than what can be explained by Flanagan-Clewley theory alone, and lends more credence to the Schwarz-Khachaturyan theory, which was at least able to predict within an order of magnitude of the observation.

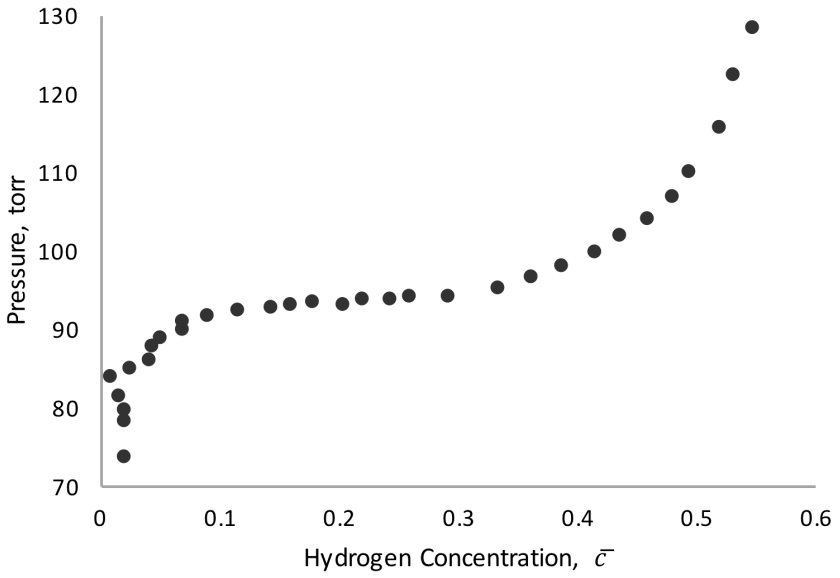

Fig 7.2. The absorption isotherm during the second cycle for the palladium-hydride system, with the two-phase region focused. Note the upward trend in the pressure during the two-phase region, which is atypical of equilibrium phase transformations.

In addition to the hysteresis gap, an interesting feature of the pressure-isotherm graph is the consistent pressure deviation during the two-phase region. During absorption, the plateau pressure *rises* very slowly at the start of the transformation and much faster near the end. The reverse is true for desorption as the pressure *drops* very slowly at the start of the transformation and much faster near the end. This effect is emphasized in Fig 7.2 above, which shows the two-phase region "plateau" during absorption. Observe that the pressure near the start of the phase transition is around 90 torr, whereas it reaches 120 torr at the end. For desorption, the pressure starts around 40 torr but drops to 30 torr at the end. In thermodynamic terms, the pressure is directly

related to the chemical potential of the hydrogen gas, as repeatedly utilized in Ch 2 and 3:

$$\mu_g = \mu_g^0 + \frac{1}{2} kT \ln\left(\frac{p_g}{p_g^0}\right)$$

So, the change in the "plateau" pressure corresponds to a change in the chemical potential. During absorption, the chemical potential is seen to be rising throughout the two-phase region, whereas it is decreasing during desorption. The implications and causes of this deviation are discussed in more detail in the next chapter.

7.2 Lattice Parameters

The most common results of diffraction analyses on crystalline materials are lattice parameters, and in the context of metal hydride systems, they provide information on how the unit cell changes its size due to hydrogen uptake by the material. Lattice parameters from the analysis of the in-situ diffraction profiles are shown in Fig 7.3.

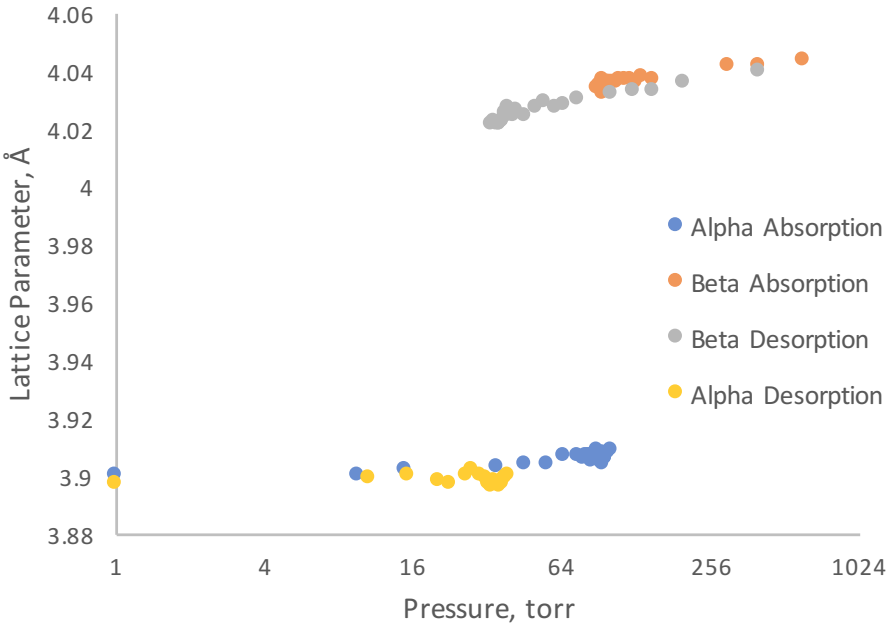

Fig 7.3. Lattice parameters of α and β phase during the second cycle of the palladium hydride system, plotted versus pressure. Lattice parameters are color coded by phase and transformation direction.

At first glance, the lattice parameters for both phases are along the same range during absorption and desorption for each phase: ~3.9 Å for α and 4.04 Å for β. There are large clusters of points around the two-phase regions for absorption and desorption for each phase. This is as expected for a typical phase transformation theory, as the lattice, and by extension an entire phase, should not be changing in its structure or composition during a phase transformation. To elucidate the behavior of the lattice parameter among these clusters, the lattice parameter is now plotted versus the concentration of hydrogen uptake:

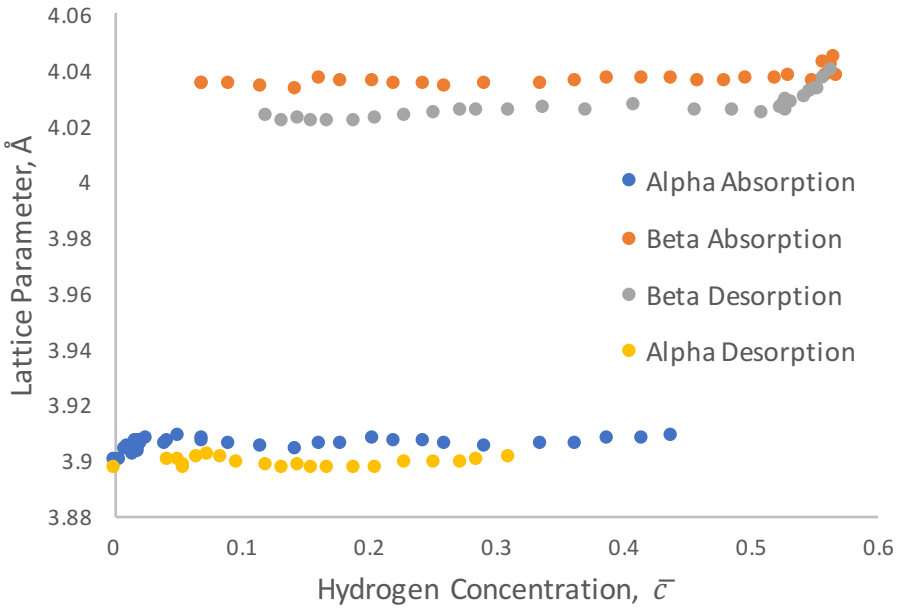

Fig 7.4. Lattice parameters of α and β phase during the second cycle of the palladium hydride system, plotted versus hydrogen concentration. Note the discrepancies in the lattice parameter during absorption and desorption within each phase.

Since hydrogen uptake is largest during the phase transformation, the modification of using concentration instead of pressure as the horizontal axis in Fig 7.4 serves to expand the clustered points from Fig 7.3. Now, it is clear that the α phase lattice parameter is higher during absorption than for desorption. The same also occurs for the β phase lattice parameter. The main lattice parameters that can be viewed in Fig 7.4 are

those from the two-phase region, so it is the two-phase region where a discrepancy in lattice parameter can be seen. Recall that such an effect was not prominent in Fig 7.3, where the lattice parameter was shown versus pressure. To understand this supposed 'hysteresis' in the lattice parameter, consider the focused lattice parameters of just one phase in Fig 7.5:

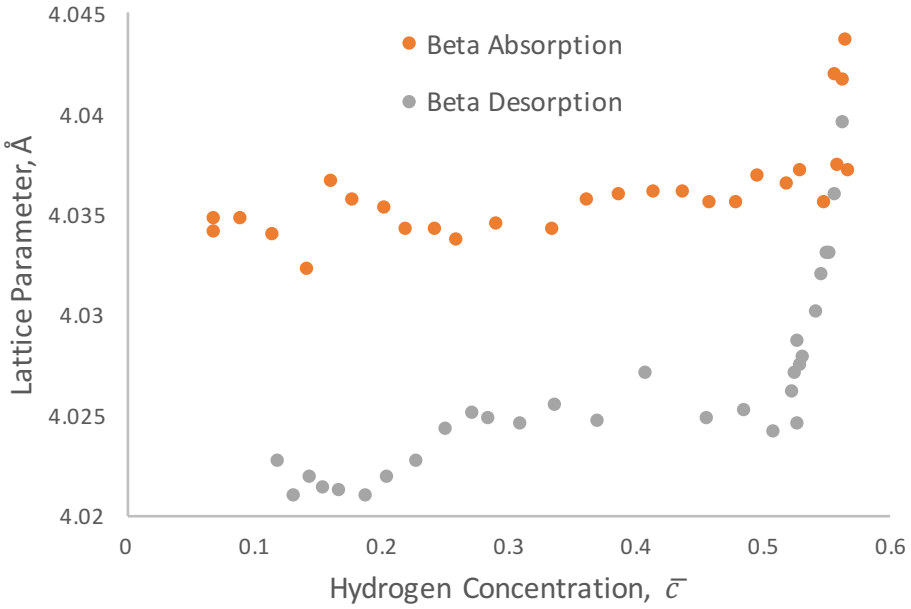

Fig 7.5. Lattice parameters of the β phase during the second cycle of the palladium hydride system, plotted versus hydrogen concentration. Observe that the lattice parameters appear close to constant in the two-phase region, but they are higher for absorption than for desorption.

Fig 7.5 gives clues to the origin of the supposed lattice parameter 'hysteresis'. Observe the strong linearity of the lattice parameter with respect to concentration in the pure β phase regime on the far-right portion of the figure. This is an occurrence of the same Vegard's law that was introduced in the theoretical discussions of Ch 2:

$$a = (1 + \varepsilon_0 \bar{c}) a^0$$

The lattice parameter is thus linearly related to the concentration of hydrogen interstitial atoms. As seen in Fig 7.1, due to the pressure hysteresis, the absorption plateau

occurs at a higher pressure than for desorption. This also leads to higher hydrogen concentrations in both phases during the absorption plateau than for desorption. Hence, Vegard's law predicts that the lattice parameters during the absorption plateau will be higher than those for the desorption plateau.

Both the original Schwartz-Khachaturyan and Flanagan-Clewley theories predict the same general shape for a pressure-concentration curve hysteresis, so when used in conjunction with Vegard's law, both of these theories are able to predict these observed behaviors in lattice parameters in the two-phase region.

When Vegard's law is applied directly to the pure α and β phase regimes, such as the far-right portion of Fig 7.5, a consistent value for Vegard's constant of $\varepsilon_0 = 0.07$ is obtained. The application of Vegard's law to these regimes gives very strong linear fits with coefficients of determination greater that 95%. These results suggest that Vegard's law is indeed a valid approximation in the PdH system. This law is a crucial assumption in the Schwarz-Khachaturyan theory, as noted in Ch 2.

Finally, observe from Fig 7.5 that the lattice parameters in the two-phase region are not completely horizontal, but have a slight upward slope. This phenomenon is related to the deviations from constant pressure for the plateaus of the pressure-concentration isotherm, and is considered in more detail in the next chapter.

7.3 Phase fractions

Phase fractions provide an additional source of information to validate observed trends in other datasets, such as the hydrogen uptake concentrations. As introduced in Ch 2, the fraction of β phase in the two-phase region is:

$$\omega_\beta = \frac{\bar{c} - c_\alpha}{c_\beta - c_\alpha}$$

Similarly, the fraction of α phase is:

$$\omega_\alpha = 1 - \omega_\beta = \frac{c_\beta - \bar{c}}{c_\beta - c_\alpha} \tag{7.1}$$

In the two-phase plateau region, c_α and c_β are constant for typical equilibrium phase transformations. Hence, the phase fractions are directly related to $\bar{c}$. As expected, a

graph of phase fraction versus pressure is quite similar to an inverted pressure-concentration isotherm:

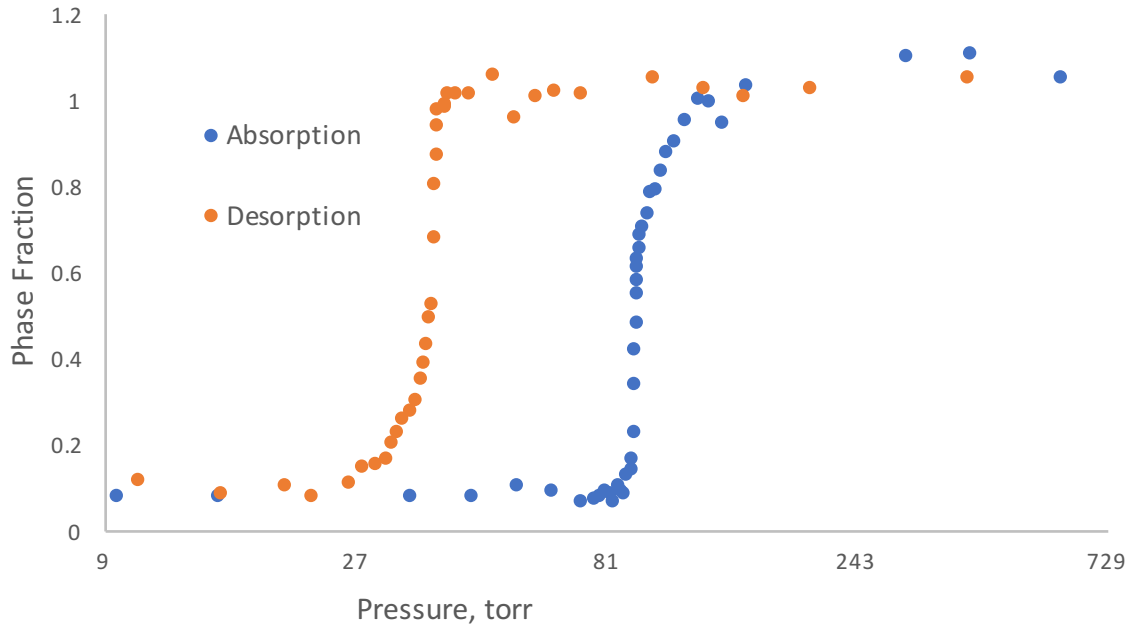

Fig 7.6. Fraction of β phase versus pressure. The graph has a logarithmically scaled horizontal axis to allow for viewing of the whole pressure range from vacuum to 700 torr.

Both the Schwarz-Khachaturyan and Flanagan theories assume that the compositions of each phase are constant during the two-phase regimes. Hence, they both predict a linear relationship between the phase fraction and concentration, in the form of the ω_α and ω_β above. In Fig 7.7, the fraction of β phase is plotted versus the hydrogen concentration. It is seen that the fraction of β phase increases as hydrogen concentration increases, consistent with the theories. However, the relationship between phase fraction and concentration is not always linear. During absorption, the phase fraction grows at a faster rate initially as hydrogen concentration increases from 0.1 to 0.5, but the increase is slowed from 0.3 to 0.5. The reverse is true for desorption: the β phase fraction drops rapidly from 0.4 to 0.3 hydrogen concentration, but the drop is slower from 0.3 to 0.1. These deviations from linearity are once again related to the deviations from constant

pressure for the plateaus of the pressure-concentration isotherm, and is considered in more detail in the next chapter. To observe the scale of these deviations, which appear with stronger magnitudes for the phase fraction dataset than other datasets, consider Fig 7.8, where the β phase fraction with pressure is analyzed specifically around the two-phase region for absorption. The deviations from typical phase transformation theory are very strongly visible in this figure, with the transformation starting near 90 torr but only concluding near 120 torr.

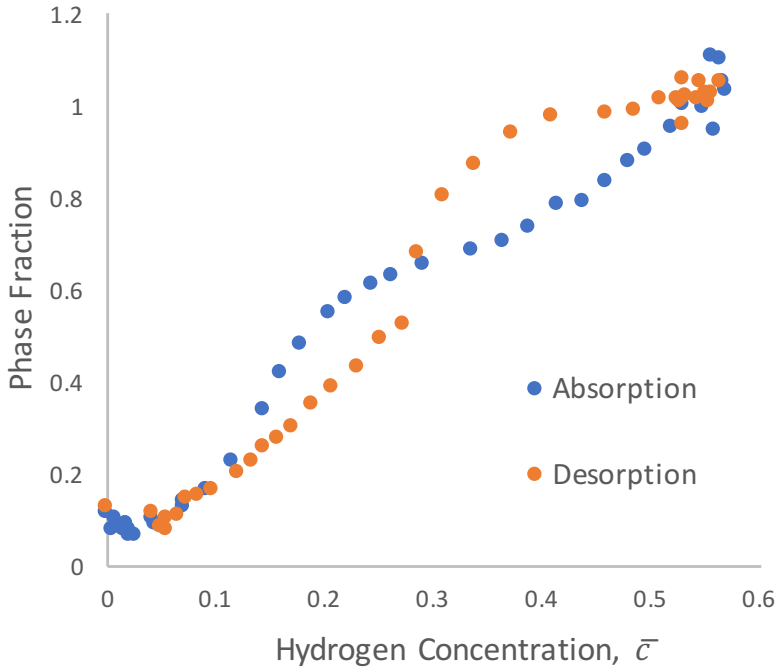

Fig 7.7. Fraction of β phase versus hydrogen concentration. In a typical phase transformation, the two curves should be close to linear.

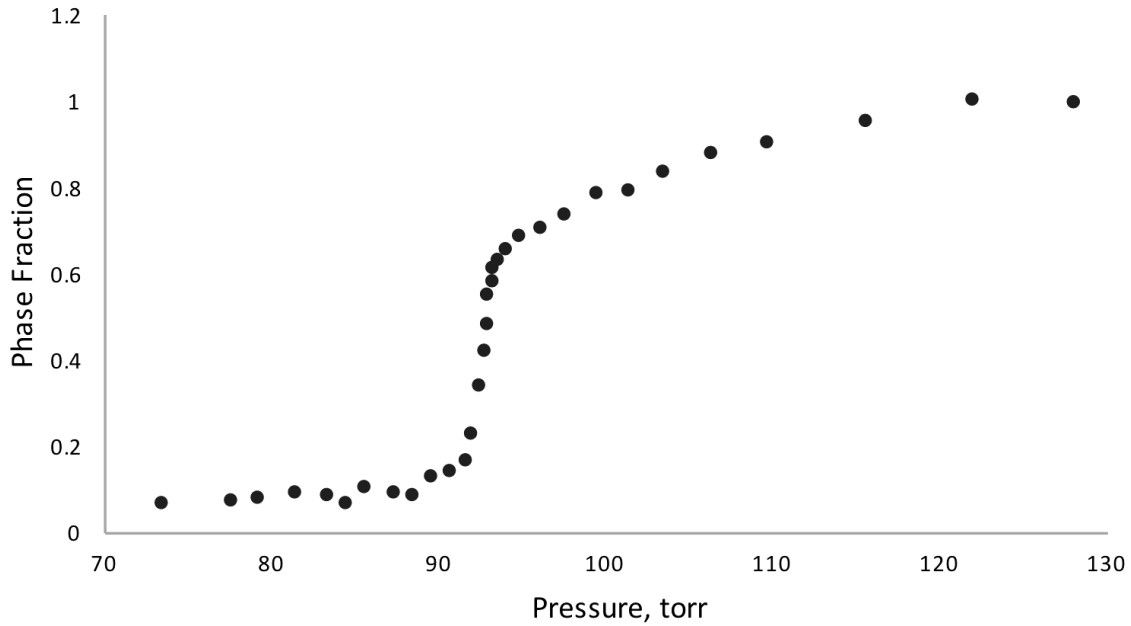

Fig 7.8. Fraction of β phase during hydrogen absorption, plotted versus pressure, with an emphasis on the two-phase region. In a typical phase transformation, the phase fraction should be nearly constant (vertical in the graph) for the whole two-phase region, which starts around 90 torr.

7.4 Microstrain

The peak broadening changes that occur over the course of the absorption and desorption phase transformation are primarily attributed to a strain-based origin. Palladium is a cubic material, and SEM images have shown that the powder particles themselves do not break apart. Hence the crystallite size broadening is negligible, and lattice strain is the most probably cause of broadening variations over the course of a cycle. Both the Schwarz-Khachaturyan and Flanagan-Clewley theories require lattice strains of some form to develop and consequently affect peak broadening.

As mentioned much earlier in the chapter, the material after the first cycle will contain more defects in its microstructure than the precursor annealed material, a fact that is acknowledge by both the Schwarz-Khachaturyan and Flanagan-Clewley theories. Strain is closely related to defect concentrations – a higher density of defects will lead to more distortion of the lattice from its theoretical crystal structure in the absence of

defects. This distortion in turn causes a local variation in atomic spacing throughout the lattice, which manifests itself in diffraction as peak broadening. The peak broadening is then connected to microstrain in the lattice on a macroscopic level. Data for microstrain of each phase from the first cycle affirm this fact experimentally, with the microstrain at the end of the first cycle much higher than at the start:

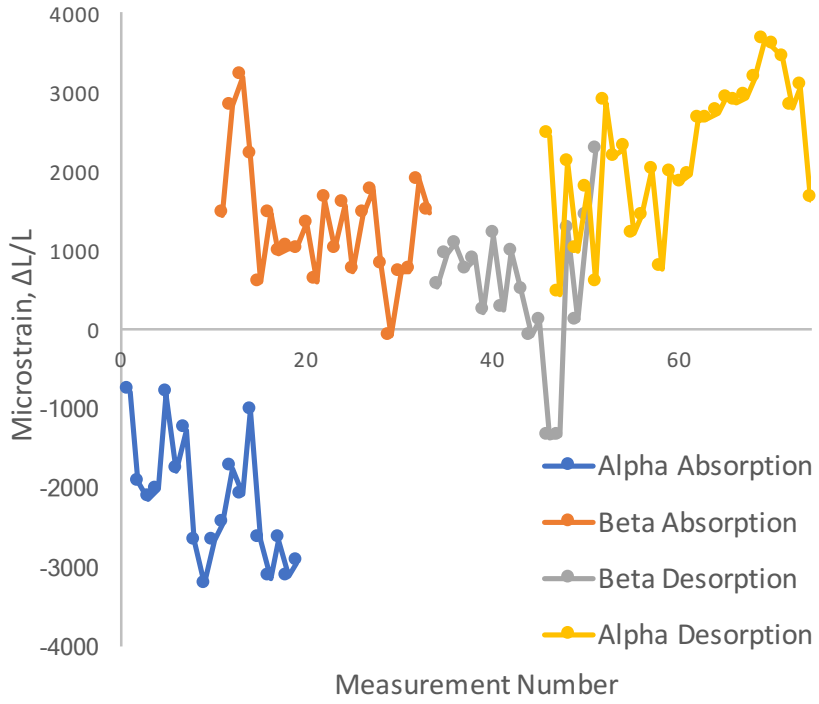

Fig 7.9. The evolution of microstrain in each phase as the first cycle progresses. Due to procedure used for instrumental parameter fitting, the vertical axis is best understood as a relative scale whose origin may not necessarily be at the 0 indicated.

Observe, from Fig 7.9, that the largest jumps in microstrain occur during the phase transformation, and the forming phase seems to be forming with a larger microstrain than that present in the disappearing phase. This is in agreement with the idea that the defect density increases in the forming phases compared to the disappearing phases (discussed in Ch 3), especially during the first cycle, since the precursor material is annealed and has a very low initial defect density.

A similar graph from the microstrain data of the second cycle presents a different story:

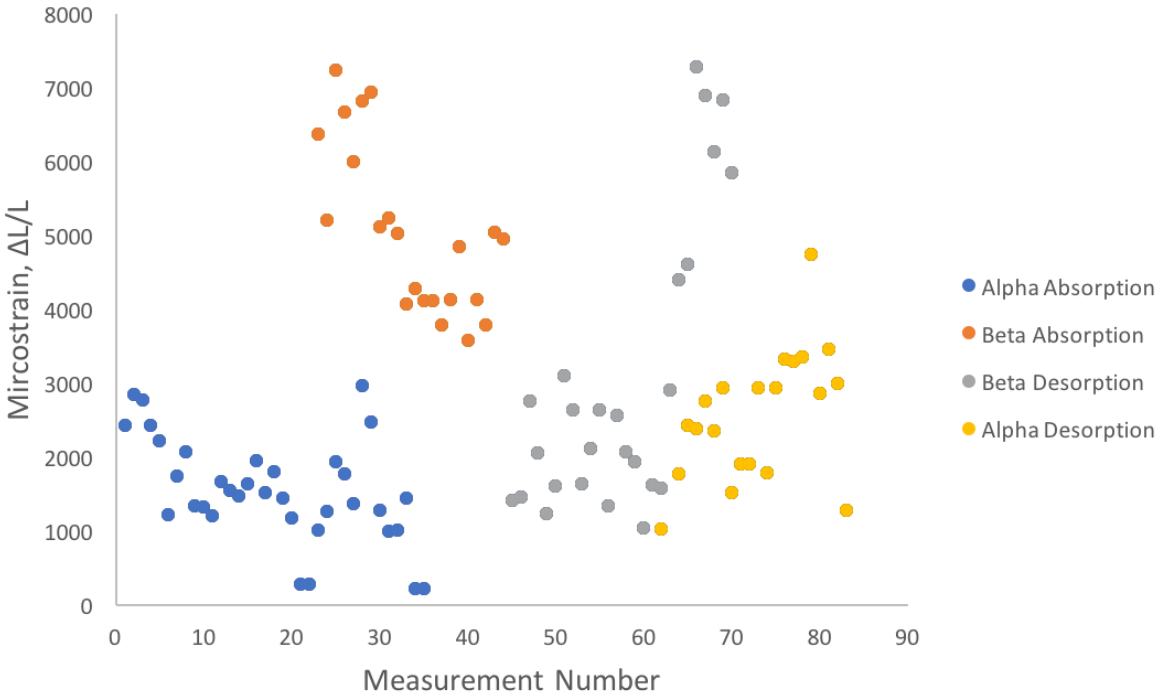

Fig 7.10. The evolution of microstrain in each phase as the second cycle progresses.

From Fig 7.10, the second cycle shows that the microstrain at the beginning and end are the same order of magnitude, indicating that the defect density is close to the same at both points. Fig 7.10 provides experimental evidence for choosing to focus analysis on the second cycle, as discussed in the beginning of this chapter. To control for the additional hysteresis component caused by the rapid increase in defect density during the first cycle, the second cycle is shown the all the figures of this chapter.

In the specific case of the Schwarz-Khachaturyan theory, strains in the material evolve over the course of cycling primarily due to the presence of misfitting hydrogen interstitial atoms. From Ch 2, the elastic strain energy created by the insertion of hydrogen atoms is:

$$e_{el} = A\bar{c}(1 - \bar{c})$$

From continuum mechanics, the elastic strain energy of a material may also be written as:

$$e_{el} = \frac{1}{2} v E \varepsilon^2 \tag{7.2}$$

where v is the molar volume, E the elastic modulus and ε the strain. Setting the two expressions equal:

$$\frac{1}{2} v E \varepsilon^2 = A\bar{c}(1-\bar{c})$$

$$\varepsilon = \sqrt{\frac{2A\bar{c}(1-\bar{c})}{vE}} \tag{7.3}$$

The most significant effect of hydrogen concentration on the strain comes from the $\bar{c}(1-\bar{c})$ term in the square root. The term leads to maxima in strain in the middle of the phase transformation, where the strain energy is highest. Hence, the Schwarz-Khachaturyan theory predicts peaks in a graph of microstrain versus hydrogen concentration. Such a graph is presented for absorption in Fig 7.11, and there do seem to be peaks for both phases around a hydrogen concentration of 0.3, following the prediction. A similar graph for desorption is also in Fig 7.11, and a peak is found around 0.25 although the relationship is more tenuous.

In the case of the Flanagan-Clewley theory, the strain energy arises from the dislocation density. The elastic energy of a single dislocation is commonly expressed as:

$$E_{disl} = \frac{1}{2} G \left|\vec{b}\right|^2 d \tag{7.4}$$

where G is the shear modulus, $\left|\vec{b}\right|$ the magnitude of the dislocation's Burgers vector and d the dislocation's length [4]. Assuming that all the dislocations in a material are similar and possess an energy of this form, the total elastic energy per unit volume for a given dislocation density, ρ, is:

$$E_{tot,disl} = \frac{1}{2} G \left|\vec{b}\right|^2 d\rho \tag{7.5}$$

This expression may be equated, as before, with the general elastic strain energy of a material:

$$\frac{1}{2} G \left|\vec{b}\right|^2 d\rho = \frac{1}{2} v E \varepsilon^2$$

$$\varepsilon = \sqrt{\frac{G\left|\vec{b}\right|^2 d\rho}{vE}} \tag{7.6}$$

As mentioned in the theoretical discussion of Ch 3, the Flanagan-Clewley theory assumes that the enthalpy for dislocation formation is constant throughout the phase transformation. For such a scenario, the dislocation density being created in the forming phase must be close to constant for the whole phase transformation. Hence, the strain expression derived above should not have any significant dependence on hydrogen concentration. There will be a very small dependence on concentration due to the molar volume v, which grows with increases in hydrogen concentration. However, within the two-phase region, v should be constant within a phase, and ε itself should be constant. The trends in microstrain found in Fig 7.11 do sometimes appear close to constant within each phase. Such an explanation would imply that the non-constant variation that is present in Fig 7.11 is either due to random error, or other affects unexplained by the Flanagan-Clewley theory. It is more likely that the deviations from a constant strain are from unexplained effects due to the presence of discernible trends in the deviations.

As additionally mentioned in the theoretical discussion of Ch 3, the dislocation density is likely not a constant in the forming phase during the transformation. Instead, it increases up to the dislocation density of a work-hardened metal at the end of the transformation. As dislocations are primarily produced in the forming phase according to Flanagan-Clewley theory, the strains in the α phase during absorption and β phase during desorption should be close to constant. Using the expression for strain calculated above, the strains in the β phase during absorption and α phase during desorption should be increasing throughout the transformation. In terms of concentration, the microstrain in the β phase during absorption should rise with increasing hydrogen concentration and that in the α phase during desorption should rise with decreasing hydrogen concentration. These predictions are not noticeably supported by the data of Fig 7.11.

The behavior of microstrain during cycling is better explained by the Schwarz-Khachaturyan theory than by the Flanagan-Clewley theory. This may be for the same

reason as the hysteresis gap size: the effects predicted by Flanagan-Clewley theory are an order of magnitude smaller than those of the Schwarz-Khachaturyan theory.

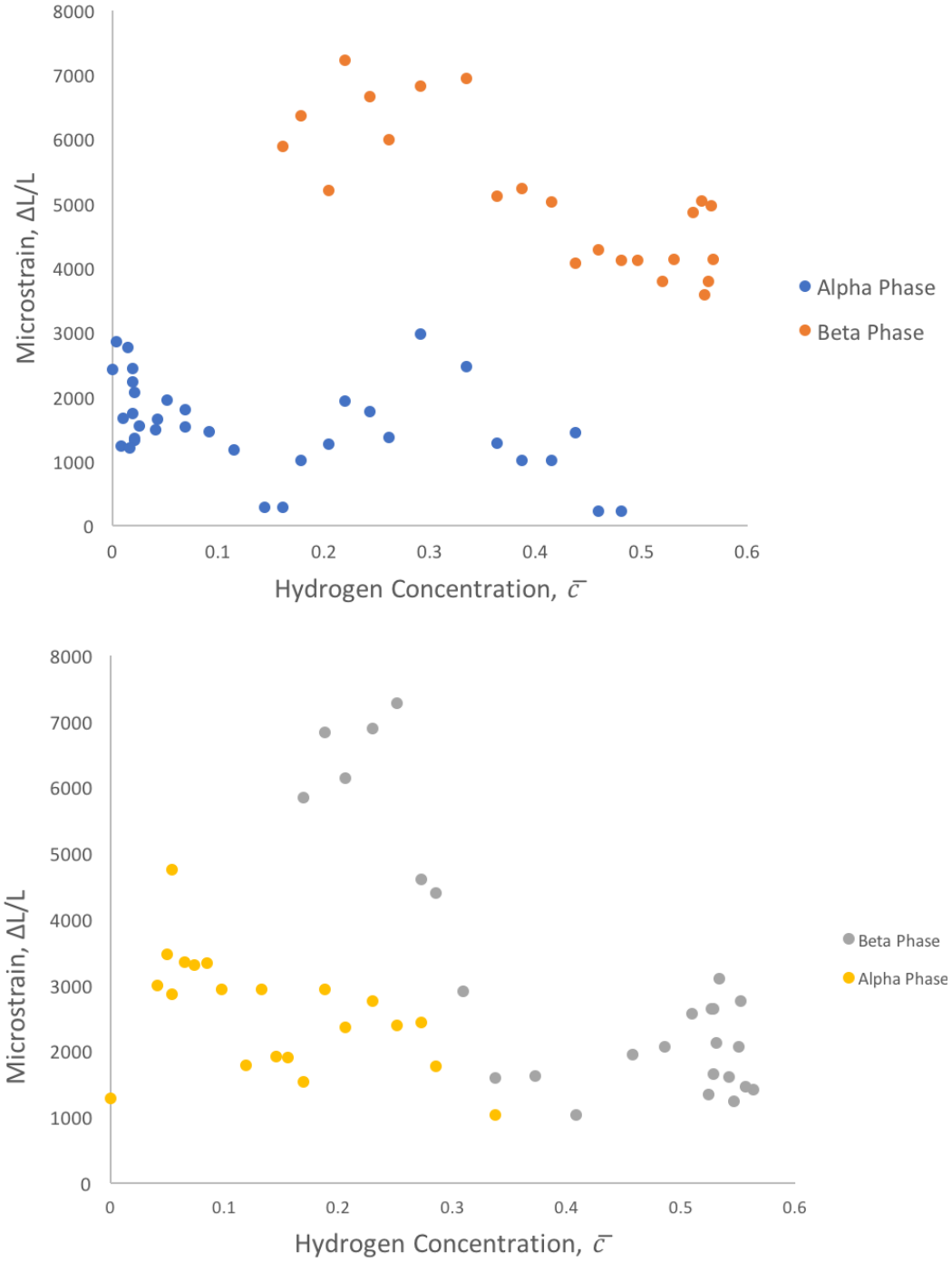

Fig 7.11. Graph of microstrain versus hydrogen concentration, for the absorption (above) and desorption (below) phase transformations.

Overall, the Schwarz-Khachaturyan theory offered better predictions for the pressure-concentration hysteresis gap and strain than the Flanagan-Clewley theory, whereas both theories had similar predictions for phase fractions and lattice parameters. Both theories lack the ability to describe behaviors such as the aforementioned deviations in the plateau pressure, lattice parameter and phase fraction with concentration in the two-phase region. These deviations are henceforth called the 'lingering phase', and the next chapter offers an explanation of these phenomena in a new general theory of metal hydride hysteresis.

7.5 Chapter References

1. Syrenova, S. et al. Hydride formation thermodynamics and hysteresis in individual Pd nanocrystals with different size and shape. *Nature Materials* 14, 1236-1244 (2015).
2. Ho, E., Goldberg, H., Weatherly, G. & Manchester, F. An in-situ electron microscope study of precipitation in palladium-hydrogen alloys. *Acta Metallurgica* 27, 841-853 (1979).
3. Bever, M., Holt, D. & Titchener, A. The stored energy of cold work. *Progress in Materials Science* 17, 5-177 (1973).
4. Ladd, A. & Hoover, W. Energy and entropy of interacting dislocations. *Physical Review B* 26, 5469-5479 (1982).

Chapter VIII

Combined General Theory of Hysteresis

As seen in the previous chapter, the Schwarz-Khachaturyan and Flanagan-Clewley theories explain parts of the data to varying degrees. However, the observed hysteresis gap is only half of the value predicted by Schwarz-Khachaturyan theory. Additionally, the lingering phase behaviors observed in the pressure-concentration isotherms, lattice parameters and phase fractions remain unexplained. As seen in Fig 7.2, 7.5 and 7.8, these effects are large enough to represent a significant gap in the understanding of metal hydride materials. They represent strong deviations from the typical theory of phase transformations where transformations are supposed to occur at fixed temperature and pressure conditions, which is required by the Gibbs phase rule.

As agreed by several authors in the field, defect densities play a role in the formation of hysteresis gaps even though the discussion of the previous chapter has shown that the Schwarz-Khachaturyan theory was able to explain more effects than the Flanagan-Clewley theory [1-4]. In addition, at the end of Ch 3, it was noted that an extension to the Flanagan-Clewley theory to allow for a decreasing dislocation formation energy with work hardening can explain deviations in the chemical potential, and in turn in the pressure, during the two-phase region. This suggests a combined approach of the two theories may be beneficial.

8.1 Combined Thermodynamics

To derive a general theory incorporating all the possible effects arising from both defects and the strain of misfitting particles, consider a combined Gibbs free energy formulation that includes both effects:

$$g_{2ph,abs} = g_{chem,\alpha}(c_\alpha)(1-\omega) + g_{chem,\beta}(c_\beta)\omega + e_\alpha + e_\beta + e_{\frac{\alpha}{\beta}} + \Delta h_{disl} * \omega \quad (8.1)$$

$$g_{2ph,des} = g_{chem,\alpha}(c_\alpha)(1-\omega) + g_{chem,\beta}(c_\beta)\omega + e_\alpha + e_\beta + e_{\alpha/\beta} + \Delta h_{disl} * (1-\omega)$$

where the terminology used is the same as in Ch 2 and 3. There are 2 separate Gibbs free energies for the absorption two-phase region and the desorption two-phase region because the formation of dislocations affects them differently as outlined in Ch 3. To incorporate real-world variations from ideal behavior, as mentioned at the end of Ch 3, allow Δh_{disl} to be a monotonic increasing function of the extent of transformation. Δh_{disl} grows with increasing hydrogen concentration during absorption, while it grows with decreasing concentration during desorption. During absorption, the extent of transformation is ω, whereas it is $(1 - \omega)$ during desorption. Δh_{disl} may be written as functions of these values for the respective parts of the cycle. In addition, as mentioned at the end of Ch 2, the coherency of the phase boundary can be accounted for with the modification $e_{\alpha/\beta} \rightarrow e_{\alpha/\beta}\phi$, where $\phi = 1$ represents a fully coherent interface and $\phi = 0$ represents a fully incoherent interface. ϕ may itself be some function of hydrogen concentration. If it is, assume that it is symmetric with respect to the extent of reaction. Since the α and β phases are very similar structurally in the case of palladium hydride, this is a reasonable assumption. The value of ϕ for $\omega \ll 1$ should be the same as the value of ϕ for $(1 - \omega) \ll 1$. In the beginning and end of the transformation the interface is likely to be the most coherent as one phase is much smaller than the other and can hence easily connect to the lattice of the other at an interface. In the middle of the transformation, the interface is likely to be the most incoherent as both phases have similarly-sized regions. So, ϕ may have a minimum in the middle of the transformation while remaining a symmetric function about the vertical axis of that minimum. For the immediately following discussion, assume for simplicity that ϕ is very close to constant. Also, assume that the effects due to variation of the volume of the occupied hydrogen lattice site that are mentioned in Ch 2 are not appreciable enough to be manifested in the available datasets, because the lattice parameter only grows by 3.9% during the phase transformation. Hence,

$$g_{2ph,abs} = g_{chem,\alpha}(c_\alpha)(1-\omega) + g_{chem,\beta}(c_\beta)\omega + e_\alpha + e_\beta + e_{\alpha/\beta}\phi + \Delta h_{disl}(\omega) * \omega$$

$$g_{2ph,des} = g_{chem,\alpha}(c_\alpha)(1-\omega) + g_{chem,\beta}(c_\beta)\omega + e_\alpha + e_\beta + e_{\frac{\alpha}{\beta}}\phi + \Delta h_{disl}(1-\omega) * (1-\omega) \quad (8.2)$$

The expression $e_\alpha + e_\beta + e_{\alpha/\beta}\phi$ may be expanded as $Ac_\alpha(1-c_\alpha)\omega + Ac_\beta(1-c_\beta)(1-\omega) + A(c_\beta - c_\alpha)^2\,\omega(1-\omega)\phi$:

$$g_{2ph,abs} = g_{chem,\alpha}(c_\alpha)(1-\omega) + g_{chem,\beta}(c_\beta)\omega + Ac_\alpha(1-c_\alpha)\omega + Ac_\beta(1-c_\beta)(1-\omega) + A(c_\beta - c_\alpha)^2\,\omega(1-\omega)\phi + \Delta h_{disl}(\omega) * \omega$$

$$g_{2ph,des} = g_{chem,\alpha}(c_\alpha)(1-\omega) + g_{chem,\beta}(c_\beta)\omega + Ac_\alpha(1-c_\alpha)\omega + Ac_\beta(1-c_\beta)(1-\omega) + A(c_\beta - c_\alpha)^2\,\omega(1-\omega)\phi + \Delta h_{disl}(1-\omega) * (1-\omega) \quad (8.3)$$

Consider the chemical potential during the absorption two-phase region:

$$\mu_{2ph,abs}(\bar{c}) = \frac{dg_{2ph,abs}(\bar{c})}{d\bar{c}}$$

$$= \left(g_{chem,\beta}(c_\beta) + Ac_\alpha(1-c_\alpha) - g_{chem,\alpha}(c_\alpha) - Ac_\beta(1-c_\beta)\right)\frac{d\omega}{dc} + A(c_\beta - c_\alpha)^2\,\phi(1-2\omega)\frac{d\omega}{dc} + \Delta h_{disl}(\omega) * \frac{d\omega}{dc} + \frac{d\Delta h_{disl}(\omega)}{dc}\omega$$

$$= \left(g_{chem,\beta}(c_\beta) + Ac_\alpha(1-c_\alpha) - g_{chem,\alpha}(c_\alpha) - Ac_\beta(1-c_\beta)\right)\frac{1}{c_\beta - c_\alpha} + A(c_\beta - c_\alpha)^2\,\phi(1-2\omega)\frac{1}{c_\beta - c_\alpha} + \Delta h_{disl}(\omega) * \frac{1}{c_\beta - c_\alpha} + \frac{d\Delta h_{disl}(\omega)}{dc}\frac{\bar{c} - c_\alpha}{c_\beta - c_\alpha}$$

$$= \frac{1}{c_\beta - c_\alpha}\left(g_{chem,\beta}(c_\beta) + Ac_\alpha(1-c_\alpha) - g_{chem,\alpha}(c_\alpha) - Ac_\beta(1-c_\beta) + A(c_\beta - c_\alpha)^2\,\phi(1-2\omega) + \Delta h_{disl}(\omega) + \frac{d\Delta h_{disl}(\omega)}{dc}(\bar{c} - c_\alpha)\right) \quad (8.4)$$

Now, consider the chemical potential during the desorption two-phase region:

$$\mu_{2ph,des}(\bar{c}) = \frac{dg_{2ph,des}(\bar{c})}{d\bar{c}}$$

$$= \left(g_{chem,\beta}(c_\beta) + Ac_\alpha(1-c_\alpha) - g_{chem,\alpha}(c_\alpha) - Ac_\beta(1-c_\beta)\right)\frac{d\omega}{dc} + A(c_\beta - c_\alpha)^2\,\phi(1-2\omega)\frac{d\omega}{dc} - \Delta h_{disl}(1-\omega) * \frac{d\omega}{dc} + \frac{d\Delta h_{disl}(1-\omega)}{dc}(1-\omega)$$

$$= \left(g_{chem,\beta}(c_\beta) + Ac_\alpha(1-c_\alpha) - g_{chem,\alpha}(c_\alpha) - Ac_\beta(1-c_\beta)\right)\frac{1}{c_\beta - c_\alpha}$$
$$+ A(c_\beta - c_\alpha)^2\,\phi(1-2\omega)\frac{1}{c_\beta - c_\alpha} - \Delta h_{disl}(1-\omega) * \frac{1}{c_\beta - c_\alpha}$$
$$+ \frac{d\Delta h_{disl}(1-\omega)}{dc}\frac{c_\beta - \bar{c}}{c_\beta - c_\alpha}$$

$$= \frac{1}{c_\beta - c_\alpha}(g_{chem,\beta}(c_\beta) + Ac_\alpha(1-c_\alpha) - g_{chem,\alpha}(c_\alpha) - Ac_\beta(1-c_\beta)$$
$$+A(c_\beta - c_\alpha)^2\,\phi(1-2\omega) - \Delta h_{disl}(1-\omega) + \frac{d\Delta h_{disl}(1-\omega)}{dc}(c_\beta - \bar{c})) \qquad (8.5)$$

As before with the Schwarz-Khachaturyan theory, observe that the misfitting particle strains cause a linear dependence of $A(c_\beta - c_\alpha)^2\,\phi(1-2\omega)$ in the expressions for the Gibbs free energy in the two-phase region.

8.2 Formulation of Pressure Hysteresis

Once again, the hysteresis gap can be calculated by subtracting the chemical potential at the start of desorption from that at the start of absorption:

$$\mu_{2ph,abs}(c_\alpha) - \mu_{2ph,des}(c_\beta)$$
$$= \frac{1}{c_\beta - c_\alpha}\left(g_{chem,\beta}(c_\beta) + Ac_\alpha(1-c_\alpha) - g_{chem,\alpha}(c_\alpha) - Ac_\beta(1-c_\beta)\right.$$
$$\left. + A(c_\beta - c_\alpha)^2\,\phi * (1) + \Delta h_{disl}(0) + \frac{d\Delta h_{disl}(0)}{dc}(c_\alpha - c_\alpha)\right)$$
$$- \frac{1}{c_\beta - c_\alpha}\left(g_{chem,\beta}(c_\beta) + Ac_\alpha(1-c_\alpha) - g_{chem,\alpha}(c_\alpha) - Ac_\beta(1-c_\beta)\right.$$
$$\left. + A(c_\beta - c_\alpha)^2\,\phi * (-1) - \Delta h_{disl}(0) + \frac{d\Delta h_{disl}(0)}{dc}(c_\beta - c_\beta)\right)$$
$$= \frac{2}{c_\beta - c_\alpha}\left(A(c_\beta - c_\alpha)^2\,\phi + \Delta h_{disl}(0)\right) \qquad (8.6)$$

The chemical potential of the hydrogen gas is also in equilibrium with the chemical potentials of the hydrogen in the two phases, which can be used to equate the above chemical potential difference to a pressure difference, as done in the theoretical discussion of Ch 2 and 3.

$$\frac{1}{2}kT\ln\left(\frac{p_g^{abs}}{p_g^{des}}\right) = \mu_{2ph,abs}(c_\alpha) - \mu_{2ph,des}(c_\beta) = \frac{2}{c_\beta - c_\alpha}(A(c_\beta - c_\alpha)^2\,\phi + \Delta h_{disl}(0))$$

$$\ln\left(\frac{p_g^{abs}}{p_g^{des}}\right) = \frac{4}{(c_\beta - c_\alpha)kT}\left(A(c_\beta - c_\alpha)^2\,\phi + \Delta h_{disl}(0)\right)$$

$$= \frac{2}{c_\beta - c_\alpha}\left(A(c_\beta - c_\alpha)^2\,\phi + \Delta h_{disl}(0)\right) \tag{8.7}$$

Observe the similarity of this expression with the hysteresis expressions derived in Ch 2 and 3.

8.3 Interface Coherency

The p_g^{abs} and p_g^{des} in the hysteresis expression of the previous section specifically correspond to the pressure at the start of absorption and at the start of desorption respectively. Hence this expression does not itself account for the lingering phase. However, it does provide a framework for explaining why the hysteresis gap ($\ln\left(\frac{p_{g,obs}^{abs}}{p_{g,obs}^{des}}\right) = .92$, from Ch 7) is less than half the size of that predicted by the Schwarz-Khachaturyan theory and an order of magnitude more than that predicted by the Flanagan-Clewley theory, which is noted in the previous chapter. $\Delta h_{disl}(0)$ corresponds to a forming phase with very few defects since it has formed very little when the extent of transformation is 0, and is much smaller than near the end of the transformation. Extending the comparisons of hysteresis gaps of Ch 7, $\Delta h_{disl}(0)$ is likely an order of magnitude lower than $A(c_\beta - c_\alpha)^2\,\phi$, so the $A(c_\beta - c_\alpha)^2\,\phi$ contributes more to the hysteresis, and $\Delta h_{disl}(0)$ can be ignored for an estimation. From Ch 7, we had that the predicted gap from Schwarz-Khachaturyan theory was:

$$\ln\left(\frac{p_{g,SK}^{abs}}{p_{g,SK}^{des}}\right) = \frac{4}{kT}\left(A(c_\beta - c_\alpha)\right) = 2.6$$

Then, equating to the observed gap:

$$0.92 \approx \frac{4}{(c_\beta - c_\alpha)kT}\left(A(c_\beta - c_\alpha)^2\,\phi\right) = 2.6\phi$$

$$\phi \approx \frac{0.92}{2.6} = 0.35$$

The parameter ϕ quantifies the extent of coherency of the interfaces of the two phases. A value of $\phi = 0.35$ may suggest that the effects of coherent boundaries are present but are significantly diminished by the lattice mismatch, which causes geometrically-necessary dislocations to form. This has been mentioned at the start of Ch 2, where the lattice mismatch was said to cause a semi-coherent phase boundary. The $\phi = 0.35$ value gives evidence of this semi-coherent nature. If the boundaries were coherent, we would have ϕ much closer to 1. Additionally, this discovery follows the results of a previous in situ TEM study on palladium hydride that has shown that the boundaries have both coherent and incoherent characteristics and may even evolve between the two [5].

8.4 Lingering Phase Behavior Explanation

The lingering phase behaviors can be explained from a purely mathematical perspective in two possible ways using the chemical potentials previously derived for the two-phase regions, since there are two parameters that could potentially vary to the extent necessary: Δh_{disl} and ϕ. The first way is the extension to Flanagan-Clewley theory presented at the end of Ch 3: allowing Δh_{disl} to be a monotonic increasing function of the extent of transformation, because the forming phase has the defect densities of a work-hardened material once the transformation is complete. As the transformation progresses, the requirement of dislocation formation becomes a continually higher barrier to the transformation. The increase in Δh_{disl} causes the chemical potential to rise during the absorption two-phase region and fall during the desorption two-phase region. The other explanation is to allow ϕ to increase with hydrogen concentration. This will have the same qualitative effect on the chemical potentials at either end of the two-phase

region as the changes in Δh_{disl}. However, the predicted pressure-isotherms would be different in shape as shown in Fig 8.1:

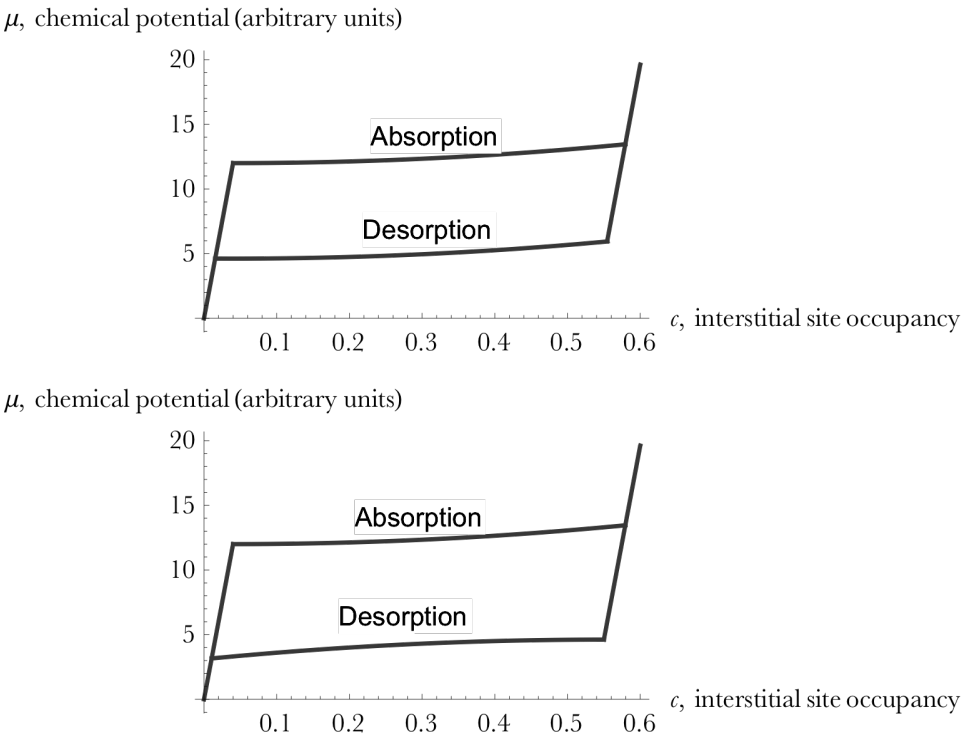

Fig 8.1. Pressure-concentration isotherm predicted by an increase in ϕ with hydrogen concentration (above) and an increase in Δh_{disl} with the extent of reaction (below).

Observe that the absorption and desorption 'plateaus' in Fig 8.1 have the same form for the prediction of a varying ϕ, whereas they have an antisymmetric form for the varying Δh_{disl} prediction. From the experimental pressure concentration isotherm of Fig 7.1 and even the phase fraction-pressure graph of Fig 7.6, it appears that the two plateaus have more of an antisymmetric form. The deviation from a constant plateau becomes stronger with greater extent of the transformation, not the hydrogen concentration. This suggests that the variation in Δh_{disl} is the most plausible explanation for the lingering phase behaviors.

With this explanation for the lingering phase, it is now possible to explain the lingering phase behaviors observed in the other datasets: lattice parameters, and phase

fractions. In Fig 7.5, the β lattice parameter shows a perceivable drop at lower hydrogen concentrations during desorption. Similarly, a perceivable increase is observed for the α lattice parameter during absorption. The lattice parameters tend to significantly deviate only when nearing the end of the phase transformation, similar to the behavior in pressures explained above. It can be observed with Vegard's law:

$$a = (1 + \varepsilon_0 c)a^0$$

In the case of the lingering phase, the hydrogen concentration of the α phase gradually increases in the plateau due to the increase in chemical potential of the plateau. Since lattice parameter is linearly related to the concentration by Vegard's law, a similar uptick is observed. The effect on the β lattice parameter can be analogously explained.

At first glance, since the phase fraction is directly related to the hydrogen concentration, it may appear that there should be no deviation in the phase fraction versus concentration graph, because any lingering phase effects are accounted for with the concentration axis that already possess the same effect. However, the correlation between phase fraction and concentration is also mediated by the compositions of the phases. The β phase fraction is presented here to follow the results of Fig 7.7:

$$\omega_\beta = \frac{\bar{c} - c_\alpha}{c_\beta - c_\alpha}$$

Both c_α and c_β are altered from the lingering phase effect. Assume that both are altered similarly, so that $c_\beta - c_\alpha \ll 1$. This is a valid assumption when the pure phase chemical Gibbs free energies of the two phases are similar: in the case of palladium, this may hold because the lattice parameters are close and the same lattice structure is present. Observe, during absorption, as $\bar{c}$ increases, c_α also increases with a growing rate. At the beginning of the phase transformation, the phase fraction will grow the fastest with concentration, because c_α is growing the slowest with concentration. Conversely, near the end of the phase transformation c_α is growing the fastest due to the lingering phase effect, and the phase fraction grows the slowest. During desorption, as $\bar{c}$ decreases, c_α decreases at a growing rate. At the beginning of the phase transformation, the phase fraction will decrease the fastest with concentration, because c_α is decreasing the slowest with concentration. Conversely, near the end of the phase transformation c_α is decreasing the

fastest due to the lingering phase effect, and hence the phase fraction decreases the slowest. These are the exact departures from perfect linearity observed in Fig 7.7, so all the deviations from normal phase transformation behavior of the phase fraction are justified by the explanation of the lingering phase effects.

8.5 Evidence from the Minor Loop

Analysis of the minor loop provides a useful dataset to test some specific predictions of the general theory of hysteresis formulated above, including the explanation for the lingering phase. During the minor loop, the extent of the absorption phase transformation was stopped at 70% conversion, when desorption was started. The material used had also previously been cycled, so the starting α phase would have a high dislocation density on the order of that of a cold worked material. So, as the β phase formed during absorption, dislocations would be produced, slowly raising Δh_{disl}. However, the dislocation densities would not reach their highest value reach during a full absorption, so the complete lingering phase behavior is not observed. Then, to reach the desorption two-phase region, the pressure must be lowered due to the barriers to phase transformation from the misfitting particle and dislocation effects, until the chemical potentials of the phases intersect $\mu_{2ph,des}(\bar{c})$. The hydrogen concentration of β phase where this occurs is higher than the usual desorption concentration of β phase for a full cycle, since $\mu_{2ph,des}(\bar{c})$ has a negative slope from the misfitting strain term. For the same reason that the hysteresis predicted by Schwarz-Khachaturyan theory is much larger than that predicted by the Flanagan-Clewley theory, this effect is larger than the contribution of the increased value of Δh_{disl} in the remaining α phase, so an appreciable increase in desorption plateau pressure compared to a full cycle should be observed. Also, during the desorption two-phase region, the already high Δh_{disl} can no longer increase appreciably because the material is work-hardened. So, there would be no significant lingering phase behavior observed during desorption. These predictions are affirmed by the experimental data, which is summarized through a phase-fraction-pressure graph to emphasize the important features:

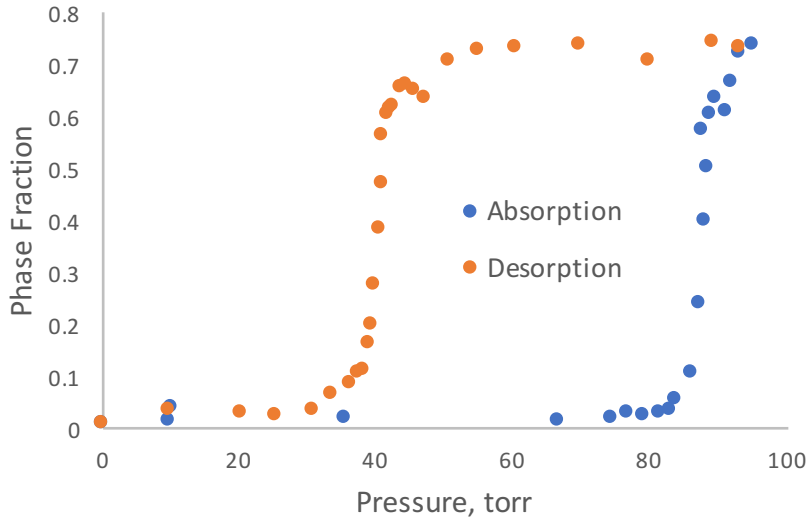

Fig 8.2. Fraction of β phase versus pressure for the minor loop. Compare this figure with Fig 7.6 and 7.8 to compare the extents of the lingering phase effect for both full cycle and the minor loop.

As predicted, in Fig 8.2, we can only see a very small amount of the lingering phase behavior during absorption, for phase fractions greater than about 0.6. The hysteresis gap is slightly smaller because the desorption plateau occurs at a higher pressure of 41 torr, than the full cycle desorption plateau measured at 37.5 torr, as predicted above. Similarly, during desorption, the lingering phase behavior is much smaller than what is observed during the full cycle (Fig 7.8). For example, in the full cycle, a pressure of 30 torr is observed around a phase fraction of 0.2, but in the case of the minor loop, a much higher pressure around 40 torr is observed for a phase fraction of 0.2.

Hence, the general theory of hysteresis formulated in this chapter is able to account for most of the observed behaviors of the PdH system with hydrogen absorption and desorption, to a greater extent than either the Schwarz-Khachaturyan or Flanagan-Clewley theories on their own.

8.6 Chapter References

1. Puls, M. Theories of Coherent Phase Equilibrium. *The Effect of Hydrogen and Hydrides on the Integrity of Zirconium Alloy Components* 207-242 (2012). doi:10.1007/978-1-4471-4195-2_7

2. Paton, N., Hickman, B. & Leslie, D. Behavior of hydrogen in α-phase Ti-Al alloys. *Metallurgical Transactions* 2, 2791-2796 (1971).
3. Gahr, S. & Birnbaum, H. Hydrogen embrittlement of niobium—III. High temperature behavior. *Acta Metallurgica* 26, 1781-1788 (1978).
4. Flanagan, T. & Clewley, J. Hysteresis in metal hydrides. *Journal of the Less Common Metals* 83, 127-141 (1982).
5. Ho, E., Goldberg, H., Weatherly, G. & Manchester, F. An in-situ electron microscope study of precipitation in palladium-hydrogen alloys. *Acta Metallurgica* 27, 841-853 (1979).

Chapter IX

Conclusions

In this study, through the process of characterizing the palladium hydride system with an in-situ x-ray diffractometer, novel data preprocessing techniques were developed, highly resolved experimental analysis showed trends unexplained by the existing literature, and a new general theoretical framework was developed to explain all the empirical observations.

Machine learning, and in particular gradient boosting with decision trees, was shown to be an effective technique for isolating specific features in a dataset. In addition, the isolation of the features was shown to be very repeatable and fast compared to manually identifying the features, once the model was trained well. In this study, machine learning was used to remove shoulder peaks from the raw data of the x-ray detector, which were caused by inaccurate time signals from the detector to the memory. The gradient boosted model was highly effective in removing the shoulder peaks, to the point where diffraction profiles from the instrument after processing with the model were almost indistinguishable from diffraction profiles acquired from a fully accurate instrument. Hence, machine learning could potentially be used in other data processing applications in material science to isolate features in a similarly fast and effective manner.

Experimentally, many of the results from the analyses of the diffraction profiles and pressure isotherms are similar to those reported in previous studies, including lattice parameters, concentrations, and phase fractions. However, for the first time, the deviation of the plateau pressure in absorption and desorption from a single pressure has been reported and analyzed to a significant level of resolution for PdH. Known as the 'lingering phase effect' in this study, it has also been shown in the lattice parameter and phase fraction data, providing more evidence for its existence. The presence of this effect suggests that more involved theories than those employed today are required to fully explain thermodynamics in metal hydrides.

Finally, from a theoretical perspective, the prediction of the strain energy-based Schwarz-Khachaturyan theory and the dislocation-based Flanagan-Clewley theory were analyzed in significant detail for the isotherm and diffraction-derived datasets. In particular, it was found that the Schwarz-Khachaturyan theory is typically better at predicting the key features of the phase transformation. However, neither theory was truly close to predicting the size of the hysteresis to reasonable accuracy, or explaining the lingering phase effect. To elucidate these unexplained features in conjunction with other observations, a new general theory of hysteresis for real metal hydride systems was formulated by combining the approaches of the Schwarz-Khachaturyan and Flanagan-Clewley theories. In addition, the extent of coherency of phase interfaces, and the variation in dislocation formation energy due to cold working, two important considerations for real-world metal hydrides, have been considered, and the resulting theory is able to explain all of the key behaviors noted in the experimental portion of this work. An important consideration for further research is to explore how effectively this model of metal hydrides can explain the thermodynamics of other common metal hydride systems.

Overall, this study has improved the understanding of real metal hydride phase transformations through a combination of experimentation and theoretical development to describe the experimental results. It provides an additional step in the understanding of the effects of hydrogen uptake in metal hydrides, and in particular, palladium. Ultimately, it provides a highly general theoretical approach for the analysis of phase transformations from hydriding in real metals.

Bibliography

Adams, B. & Chen, A. The role of palladium in a hydrogen economy. *Materials Today* 14, 282-289 (2011).

Akiba, H. et al. Nanometer-Size Effect on Hydrogen Sites in Palladium Lattice. *Journal of the American Chemical Society* 138, 10238-10243 (2016).

Andresen, A. & Maeland, A. *Hydrides for energy storage*. 395-396 (Pergamon Press, 1978).

Bever, M., Holt, D. & Titchener, A. The stored energy of cold work. *Progress in Materials Science* 17, 5-177 (1973).

Bove, R. *Modeling solid oxide fuel cells*. 13-50 (Springer, 2014).

Chen, T. & Guestrin, C. XGBoost. *Proceedings of the 22nd ACM SIGKDD International Conference on Knowledge Discovery and Data Mining - KDD '16* (2016). doi:10.1145/2939672.2939785

Chen, Z. et al. Applications of silicon nanowires functionalized with palladium nanoparticles in hydrogen sensors. *Nanotechnology* 18, 345502 (2007).

Conway, B. & Jerkiewicz, G. *Proceedings of the Symposium on Electrochemistry and Materials Science of Cathodic Hydrogen Absorption and Adsorption*. 17-26 (Electrochemical Society, 1995).

Dieter, G. *Mechanical metallurgy*. 171 (McGraw-Hill Book Company, 1961).

Eshelby, J. The Continuum Theory of Lattice Defects. *Solid State Physics* 79-144 (1956). doi:10.1016/s0081-1947(08)60132-0

Flanagan, T. & Clewley, J. Hysteresis in metal hydrides. *Journal of the Less Common Metals.* 83, 127-141 (1982).

Flanagan, T. & Kishimoto, S. Hydrogen Traps in Cold-Worked Palladium. *Electronic Structure and Properties of Hydrogen in Metals* 623-628 (1983). doi:10.1007/978-1-4684-7630-9_87

Fultz, B. *Phase transitions in materials*. (Cambridge University Press).

Fultz, B. & Howe, J. *Transmission electron microscopy and diffractometry of materials*. 17-18 (Springer, 2013).

Griessen, R., Strohfeldt, N. & Giessen, H. Thermodynamics of the hybrid interaction of hydrogen with palladium nanoparticles. *Nature Materials* 15, 311-317 (2015).

Gahr, S. & Birnbaum, H. Hydrogen embrittlement of niobium—III. High temperature behavior. *Acta Metallurgica* 26, 1781-1788 (1978).

Ho, E., Goldberg, H., Weatherly, G. & Manchester, F. An in-situ electron microscope study of precipitation in palladium-hydrogen alloys. *Acta Metallurgica* 27, 841-853 (1979).

Huang, W. et al. Experimental observation of hysteresis in a coherent metal-hydride phase transition. *Journal of Physics: Condensed Matter* 29, 495701 (2017).

Kawasaki, A. et al. Change in the crystalline structure during the phase transition of the palladium–hydrogen system. *Phys. Chem. Chem. Phys.* 17, 24783-24790 (2015).

Ladd, A. & Hoover, W. Energy and entropy of interacting dislocations. *Physical Review B* 26, 5469-5479 (1982).

Libowitz, G. The nature and properties of transition metal hydrides. *Journal of Nuclear Materials* 2, 1-22 (1960).

Lototskyy, M. et al. The use of metal hydrides in fuel cell applications. *Progress in Natural Science: Materials International* 27, 3-20 (2017).

Notten, P., Daams, J. & Einerhand, R. On the nature of the electrochemical cycling stability of non-stoichiometric LaNi5-based hydride-forming compounds Part II. In situ x-ray diffractometry. *Journal of Alloys and Compounds* 210, 233-241 (1994).

Paton, N., Hickman, B. & Leslie, D. Behavior of hydrogen in α-phase Ti-Al alloys. *Metallurgical Transactions* 2, 2791-2796 (1971).

Puls, M. Theories of Coherent Phase Equilibrium. *The Effect of Hydrogen and Hydrides on the Integrity of Zirconium Alloy Components* 207-242 (2012). doi:10.1007/978-1-4471-4195-2_7

Rowles, M. & Madsen, I. Whole-pattern profile fitting of powder diffraction data collected in parallel-beam flat-plate asymmetric reflection geometry. *Journal of Applied Crystallography* 43, 632-634 (2010).

Rusman, N. & Dahari, M. A review on the current progress of metal hydrides material for solid-state hydrogen storage applications. *International Journal of Hydrogen Energy* 41, 12108-12126 (2016).

Scholtus, N. & Hall, W. Hysteresis in the Palladium—Hydrogen System. *The Journal of Chemical Physics* 39, 868-870 (1963).

Schwarz, R. & Khachaturyan, A. Thermodynamics of Open Two-Phase Systems with Coherent Interfaces. *Physical Review Letters* 74, 2523-2526 (1995).

Schwarz, R. & Khachaturyan, A. Thermodynamics of open two-phase systems with coherent interfaces: Application to metal–hydrogen systems. *Acta Materialia* 54, 313-323 (2006).

Syrenova, S. et al. Hydride formation thermodynamics and hysteresis in individual Pd nanocrystals with different size and shape. *Nature Materials* 14, 1236-1244 (2015).

Ubbelohde, A. Some Properties of the Metallic State. I. Metallic Hydrogen and Its Alloys. *Proceedings of the Royal Society A: Mathematical, Physical and Engineering Sciences*159, 295-306 (1937).

Varoquaux, G. et al. Scikit-learn. *GetMobile: Mobile Computing and Communications* 19, 29-33 (2015).

Wadell, C. et al. Thermodynamics of hydride formation and decomposition in supported sub-10nm Pd nanoparticles of different sizes. *Chemical Physics Letters* 603, 75-81 (2014).

Wipf, H. et al. *Hydrogen in Metals III*. 279-340 (Springer Berlin, 2014).

Zang, L. *Types of Interfaces: coherent, semi-coherent, and incoherent*. at <http://www.eng.utah.edu/~lzang/images/lecture-21.pdf>

Appendix A

Machine Learning Code (Used in Chapter 5)

1. Python code to train gradient boosted decision trees on x-ray diffraction intensities

```
# shoulder deviation learning
# Aadith Moorthy – 9/22/17
import sys
import numpy as np
from sklearn.ensemble import GradientBoostingRegressor
from sklearn.externals import joblib
import matplotlib.pyplot as plt
import random
import os

# hyperparameters learned from GeO2 measurements
prediction_input_num = 100 # 100 is best while also being smaller than the first
typical peak ~9
estimators = 500 #500 best
depth = 5 # 5 and 7 were good - choose 5 for speed

# new model generator
def new_mdl():
   num_files = 22

   # process parameters to the form they should be in for the model.
   regressors = np.zeros((num_files*(4096-(prediction_input_num-1)),
prediction_input_num+1))
   fit_output_excesses = np.zeros((num_files*(4096-(prediction_input_num-1)),))
   fit_output_alls = np.zeros((num_files*(4096-(prediction_input_num-1)),))


   for file_num in range(2,2+num_files-1):
      multiplier = 10**(random.random())
      fit_output_all = np.loadtxt('Pb Slits Data/fit_output_Pbslit%d.txt' %
file_num, skiprows=1)*multiplier
```

```
        fit_output_excess = np.loadtxt('Pb Slits
Data/fit_output_shoulder_Pbslit%d.txt' % file_num,
skiprows=1)*multiplier#[0:1110]
        for i in range(0, (4096-(prediction_input_num-1))):
            regressors[(file_num-2)*(4096-(prediction_input_num-1))+i, :-1] =
fit_output_all[i:i+ prediction_input_num].copy()
            regressors[-1] = i
        fit_output_excesses[(file_num-2)*(4096-(prediction_input_num-
1)):(file_num-1)*(4096-(prediction_input_num-1))] =
fit_output_excess[prediction_input_num-1:].copy()
        fit_output_alls[(file_num-2)*(4096-(prediction_input_num-1)):(file_num-
1)*(4096-(prediction_input_num-1))] = fit_output_all[prediction_input_num-
1:].copy()

    print 'finished initializing data'

    # machine learning step
    mdl = GradientBoostingRegressor(n_estimators=estimators,
max_depth=depth)
    mdl.fit(regressors, fit_output_excesses)
    print mdl.score(regressors, fit_output_excesses)

    # visualize the fit for verification
    plt.plot(fit_output_alls)
    plt.plot(fit_output_alls-fit_output_excesses)
    plt.plot(fit_output_alls-mdl.predict(regressors))
    plt.show()
    joblib.dump(mdl, 'Pb Slits
Data/models/shoulder_model_%d_prednum_%d_estimators_%d_depth.mdl' %
(prediction_input_num, estimators, depth))

new_mdl()
```

2. Graphical user interface to remove shoulder peaks from diffraction files with the machine learned model in python

```
# shoulder remover with gui
# By Aadith Moorthy – 10/5/17
import numpy as np
from sklearn.externals import joblib
from easygui import fileopenbox, filesavebox
```

```
# hyperparameters learned from GeO2 measurements
prediction_input_num = 100 # 100 is best while also being smaller than the first
typical peak ~9
estimators = 500 #500 best
depth = 5 # 5 and 7 were good - choose 5 for speed
train = False # to force training

try:
   mdl =
joblib.load('models/shoulder_model_%d_prednum_%d_estimators_%d_depth.
mdl' % (prediction_input_num, estimators, depth))
except:
   print "Model not found"

# lab6 data test
source_file = fileopenbox(title = "Choose a file for shoulder removal. Must be in
Igor General Text Format.", default='*.txt')
real_data = np.loadtxt(source_file,skiprows=1)

regressors = np.zeros((len(real_data)-(prediction_input_num-1),
prediction_input_num+1))
for i in range(0, len(real_data)-(prediction_input_num-1)):
   regressors[i, :-1] = real_data[i:i+ prediction_input_num]
   regressors[-1] = i
res = np.concatenate((real_data[:prediction_input_num-
1],real_data[prediction_input_num-1:]-mdl.predict(regressors)))

np.savetxt(filesavebox("Save the output", default=(source_file[:-
     4]+"_shoulder_removed.txt")), res, delimiter=',')
```

Index